TWO-DIMENSIONAL MAGNETO-OPTICAL TRAP AS A LOW VELOCITY SOURCE OF ATOMIC SODIUM

by

TODD PHILIP MEYRATH, B.S., B.S.

THESIS

Presented to the Faculty of the Graduate School of

The University of Texas at Austin

in Partial Fulfillment

of the Requirements

for the Degree of

MASTER OF SCIENCE IN APPLIED PHYSICS

THE UNIVERSITY OF TEXAS AT AUSTIN

August 2000

TWO-DIMENSIONAL MAGNETO-OPTICAL TRAP AS A LOW VELOCITY SOURCE OF ATOMIC SODIUM

APPROVED BY
SUPERVISING COMMITTEE:

Supervisor: _____

Mark G. Raizen

_____

Greg O. Sitz

This thesis is dedicated to

Frank William Meyrath Jr.

and

Karen Lynn Meyrath:

my brother and sister,

my best of friends.

Acknowledgments

I would like to thank Prof. Mark Raizen for giving me the opportunity to work in his research group. Mark is full of ideas, an endless source of knowledge, and an all-around cool guy — I learned a great deal and had a lot of fun.

Thanks goes to Dr. Valery Milner for working with me on many aspects of this project and for his helpful discussions and comments. I also appreciate the suggestions and insights of the senior graduate students Martin Fischer, Daniel Steck, and Windell Oskay who are always full of knowledge and a willingness to share. The two semesters I spent as a TA in the senior lab with Braulio Gutiérrez were very educational and interesting, I'd also like to thank him for interesting discussions and suggestions. Martin and Braulio, thanks for teaching me to play soccer — maybe someday I will actually be good! Windell, movie nights were a lot of fun.

Thanks also goes to the other members of the group: Artem Dudarev, Jay Hanssen, Wes Campbell, and Kevin Henderson. Artem, thanks for all the Russian phrases. Jay, the courses we had together were interesting — I will not forget those late nights we spent with Dr. J. D. Jackson. I would also like to thank former group members Alexander Mück and Nicole Helbig for interesting discussions and insights. To all the friends I made in Austin outside of the research group, especially Adam Clark, Gauri Karve, and Todd

Tinsley — you made Austin a unique place. Thanks to everyone for putting up with my obsessively quoting movies.

T.P.M.

Austin, Texas

August 16, 2000

TWO-DIMENSIONAL MAGNETO-OPTICAL TRAP AS A LOW VELOCITY SOURCE OF ATOMIC SODIUM

Todd Philip Meyrath, M.S.Appl.Phy.
The University of Texas at Austin, 2000

Supervisor: Mark G. Raizen

This work describes the design and construction of an experimental apparatus for a two-dimensional magneto-optical trap (2D-MOT). The 2D-MOT may be used as a low velocity intense beam source of atomic sodium with application to load atom traps for novel atom optics experiments. We discuss design considerations and results obtained.

Table of Contents

List of Tables

List of Figures

xi

xii

Chapter 1

Background and Inspiration

1.1   Introduction

Generation of intense, slow atomic beams is of great interest to experiments in ultra-cold atomic physics. Such a beam may be used to load a magneto-optical trap (MOT) and a magnetic trap for evaporative cooling. One widely used method of generating slow atomic beams is the so-called Zeeman slower. In that system, the hot output of an oven is slowed by a cooling laser together with a tapered magnetic field produced by a solenoid. The Zeeman slower, however, has the undesirable property of being very bulky — a convenient and compact apparatus is preferred. Recent techniques for generating slow atomic beams involving vapor-cell MOTs have been explored by several groups [1, 2, 3]. These methods can provide atomic beams that are near the MOT capture velocity (of order $10\,\mathrm{m/s}$) without the bulk of a Zeeman slower.

This thesis describes the design and construction of an experimental apparatus for a two-dimensional magneto-optical trap (2D-MOT). We begin by giving a simple picture of the basic physics relevant to this project. In Section 1.2 there is a discussion of the basics of Doppler cooling and its limits. Doppler cooling uses spontaneous forces to dampen atomic motion (so-called *optical*

molasses). Section 1.3 extends this picture to a MOT where spontaneous forces are used to trap atoms. This is followed, in Section 1.4, by a discussion of some of the mechanisms by which atoms may be cooled below the limit of Doppler cooling. These mechanisms are due to the spatially changing polarization of the light field (polarization gradient cooling).

The essential idea of this project is to use an extension of a 2D-MOT configuration (a $2D^+$-MOT) to produce a cold atomic beam. The idea is discussed in some detail in Section 1.5.

In Chapter 2, we discuss the design and construction of different aspects of the experiment. The vacuum chamber is where the physics takes place. We discuss its components in Section 2.1. Another important aspect of the 2D-MOT is the magnetic field. A set of Ioffe coils were constructed to produce a field with a linear gradient in two dimensions and no gradient in the other. This geometry is an important part of the setup. The design of the coils and measurements of the field produced are in Section 2.2. This discussion is followed by a description of the current control electronics in Section 2.3 and optical setup in Section 2.4.

1.2   Doppler Cooling

1.2.1   Scattering Force

Consider the absorption process of a photon by a two level atom in the ground state. After the event, the internal state of the atom has changed to the excited state and the momentum of the photon is absorbed as a recoil which modifies the atom's velocity. The internally excited atom may then undergo spontaneous emission which also produces a recoil of the atom. Since spontaneous emission is equally likely in opposite directions, the recoil of a large number of spontaneous emission events averages to zero. We will call this absorption-spontaneous emission process a scattering event. The average force an atom feels due to a large number of such events is

$$\mathbf{F}_{\mathrm{sp}} = R\hbar\mathbf{k}, \tag{1.1}$$

where R is the rate of scattering. This rate is given by [4]

$$R = \frac{I\gamma/2I_{\mathrm{s}}}{1 + I/I_{\mathrm{s}} + (2\delta/\gamma)^2}, \tag{1.2}$$

where γ is the rate of decay of the excited state, I is the laser intensity, $I_{\mathrm{s}} = \pi hc/3\lambda^3\tau$ is the saturation intensity (see Table 1.2 for sodium numbers), and $\delta = \omega_{\mathrm{light}} - \omega_{\mathrm{atom}}$ is the detuning from atomic resonance.

1.2.2   Optical Molasses in 1-D

Now suppose we have a pair of counterpropagating laser beams of intensity I and frequency ω_{laser}. The laser detuning is defined as

$$\delta_{\mathrm{laser}} = \omega_{\mathrm{laser}} - \omega_{\mathrm{atom}}, \tag{1.3}$$

for which the laser is said to be *red-detuned* or *blue-detuned* for negative or positive values, respectively. More generally, since the atoms are moving, we consider an effective detuning of

$$\delta_\pm = \delta_{\text{laser}} \mp kv, \tag{1.4}$$

where the second term on the right is due to the Doppler effect. The total scattering force on an atom in this light field is the sum of the forces from each laser: $\mathbf{F} = \mathbf{F}_+ + \mathbf{F}_-$. This can be written out as

$$F(v) = \frac{1}{2}\hbar k\gamma \frac{I}{I_{\text{s}}} \left[\frac{1}{1 + I/I_{\text{s}} + (2\delta_+/\gamma)^2} - \frac{1}{1 + I/I_{\text{s}} + (2\delta_-/\gamma)^2} \right]. \tag{1.5}$$

Suppose the lasers are red-detuned (δ_{laser} is negative). In this case, we see that when an atom is moving towards the source of one of the laser beams it is closer to resonance with that beam and farther from resonance with the other beam. The atom, therefore, scatters more photons traveling in the direction opposite to atomic motion and is slowed down. We can consider this more explicitly in the small velocity limit $v \ll \delta_{\text{laser}}/k$. Equation (1.5) can be expanded to first order in v:

$$F(v) = \frac{4\hbar k(I/I_{\text{s}})(2\delta_{\text{laser}}/\gamma)}{[1 + I/I_{\text{s}} + (2\delta_{\text{laser}}/\gamma)^2]^2} \, kv. \tag{1.6}$$

Since the laser is red-detuned, Equation (1.6) describes a damping force:

$$F(v) = -\beta v. \tag{1.7}$$

With this in mind, we see that atomic motion in this laser field obeys the differential equation for particle motion in a viscous fluid. Hence, the name *optical molasses* is used [5, 6].

1.2.3   Doppler Limit

If Equation (1.6) completely described the system, then the atomic velocity would become arbitrarily close to zero given sufficient time. In this case, the ultimate temperature would be $T = 0$. However, this is not the case.

As noted in Section 1.2.1, the average change in momentum of an atom involved in a large number of spontaneous emission events in zero. However, the rms change is non-zero. One might visualize this as a random walk in momentum space, where the step size is that of the photon momentum $\hbar k$ with step frequency 2γ. From the theory of Brownian motion, the steady-state temperature is found to be

$$T_{\mathrm{D}} = \frac{\hbar\gamma}{2k_{\mathrm{B}}}. \tag{1.8}$$

This temperature is called the Doppler cooling limit (see Table 1.2 for sodium numbers) [5, 6].

1.3   A Simple Picture of the Magneto-Optical Trap

1.3.1   1D-MOT

Now, consider the situation of a two level atom with $M_{\mathrm{e}} = -1, 0, +1$ excited state Zeeman levels in a linear magnetic field given by:

$$B = G_{\mathrm{m}}z, \tag{1.9}$$

where G_{m} is the magnetic field gradient in gauss/centimeter. Suppose that we have a pair of counterpropagating circularly polarized laser beams of opposite helicity detuned by $\delta_{\mathrm{laser}} = \omega_{\mathrm{laser}} - \omega_{\mathrm{atom}}$ as in Figure 1.1. The σ_+ light
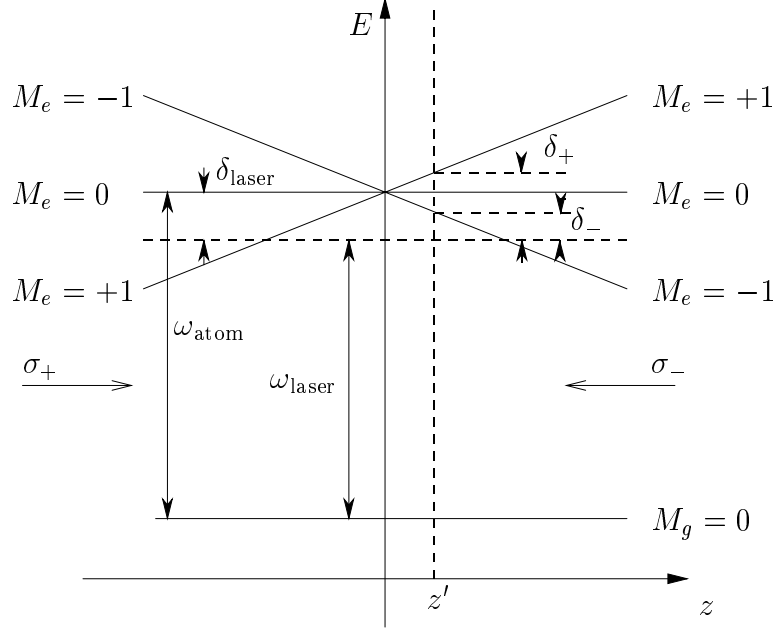
Figure 1.1: Counter propagating σ_+ and σ_- laser beams detuned from atomic resonance by $\delta_{\text{laser}} = \omega_{\text{atom}} - \omega_{\text{laser}}$ are shown. The atomic levels are shifted due to the Zeeman effect in a linear magnetic field. The effective detuning for a stationary atom at position z' is $\delta_\pm = \delta_{\text{laser}} \pm g_e \mu_B G_m z'/\hbar$ as in Equations (1.9) and (1.10).

couples to the $M_g = 0 \longrightarrow M_e = +1$ transition and the σ_- light to the $M_g = 0 \longrightarrow M_e = -1$. The effective detuning, as in Equation (1.2), is

$$\delta_\pm = \delta_{\text{laser}} \mp kv \pm (g_e M_e - g_g M_g)\mu_B B/\hbar, \qquad (1.10)$$

in general, where M_g and M_e are Zeeman sub-levels of the ground and excited states, and g_g and g_e are corresponding Landé g-factors. The second term on the right of Equation (1.10) is due to the Doppler effect and the third to the Zeeman effect. In the case of this simple example, of course, the M_g term on the right does not appear since $M_g = 0$.

The force that an atom feels in this situation is also described by Equation (1.5) but now with $\delta_\pm$ as defined in Equation (1.10) rather than Equation (1.4). This adds position dependence to F (in addition to velocity dependence):

$$F(z, v) = \frac{1}{2}\hbar k\gamma \frac{I}{I_{\mathrm{s}}} \left[\frac{1}{1 + I/I_{\mathrm{s}} + (2\delta_+/\gamma)^2} - \frac{1}{1 + I/I_{\mathrm{s}} + (2\delta_-/\gamma)^2} \right]. \quad (1.11)$$

In the small velocity and weak field limit, i.e. where $v \ll \delta_{\mathrm{laser}}/k$ and $B \ll \hbar\delta_{\mathrm{laser}}/\mu_{\mathrm{B}}$, Equation (1.11) can be expanded:

$$F(z, v) = \frac{4\hbar k(I/I_{\mathrm{s}})(2\delta_{\mathrm{laser}}/\gamma)}{[1 + I/I_{\mathrm{s}} + (2\delta_{\mathrm{laser}}/\gamma)^2]^2}(kv + (g_{\mathrm{e}}\mu_{\mathrm{B}}G_{\mathrm{m}}/\hbar)z). \quad (1.12)$$

The equation of motion is therefore:

$$\ddot{z} + \gamma_{\mathrm{trap}}\dot{z} + \omega_{\mathrm{trap}}^2 z = 0, \quad (1.13)$$

where

$$\gamma_{\mathrm{trap}} = \frac{4\hbar k^2 (I/I_{\mathrm{s}})(2(-\delta_{\mathrm{laser}})/\gamma)}{m\left[1 + I/I_{\mathrm{s}} + (2\delta_{\mathrm{laser}}/\gamma)^2\right]^2}, \quad (1.14)$$

$$\omega_{\mathrm{trap}}^2 = \frac{4\hbar k(g_{\mathrm{e}}\mu_{\mathrm{B}}G_{\mathrm{m}}/\hbar)(I/I_{\mathrm{s}})(2(-\delta_{\mathrm{laser}})/\gamma)}{m\left[1 + I/I_{\mathrm{s}} + (2\delta_{\mathrm{laser}}/\gamma)^2\right]^2}, \quad (1.15)$$

and m is the atomic mass. In a MOT, the laser detuning $\delta_{\mathrm{laser}} = \omega_{\mathrm{laser}} - \omega_{\mathrm{atom}}$ is red, so Equation (1.13) is that of a damped harmonic oscillator. This motion can be characterized by

$$\alpha \equiv \frac{\gamma_{\mathrm{trap}}^2}{4\omega_{\mathrm{trap}}^2} = \frac{\hbar k^3 (I/I_0)(2(-\delta_{\mathrm{laser}})/\gamma)}{(g_{\mathrm{e}}\mu_{\mathrm{B}}G_{\mathrm{m}}/\hbar)m\left[1 + I/I_{\mathrm{s}} + (2\delta_{\mathrm{laser}}/\gamma)^2\right]^2}. \quad (1.16)$$

In a typical experimental situation, with $G_{\mathrm{m}} \approx 10\,\mathrm{G/cm}$ and $\delta_{\mathrm{laser}} \approx 20\,\mathrm{MHz}$, α is of order 100 which clearly makes the motion strongly over damped. Any displacement therefore decays exponentially towards the center.

1.3.2 Standard 3D-MOT

One might imagine the concept of the previous section extended to three dimensions, as in Figure 1.2. The current carrying coils produce a spherical quadrupole magnetic field. Six mutually perpendicular laser beams propagate through the center of the trap. The σ_- and σ_+ polarizations are oriented so that the light couples to the down-shifted zeeman level in all directions. This configuration was first demonstrated by Raab *et al.* at AT&T Bell Labs in 1987 [7].
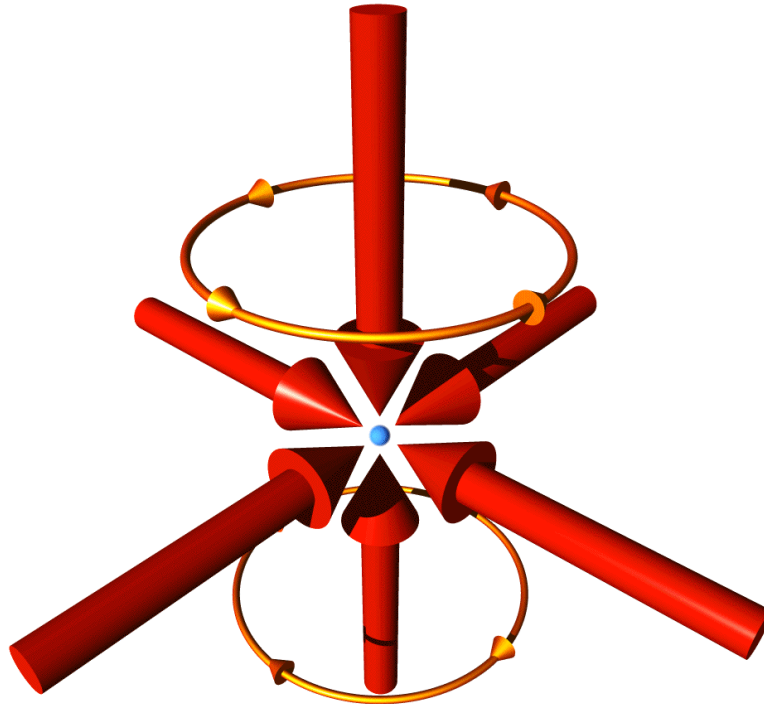
Figure 1.2: 3D-MOT pictorial. The large red arrows represent laser beams, the gold loops represent the current loops for creating the fields and the blue sphere in the center represents the trapped atoms. Drawing by Windell Oskay.
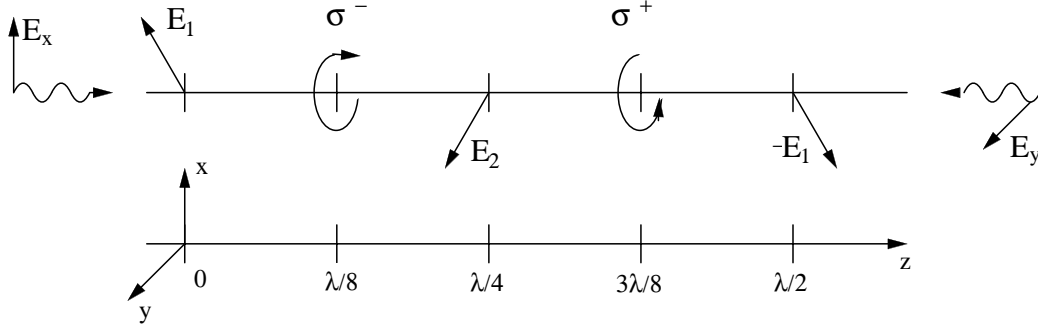
Figure 1.3: Polarization gradient in Linear $\perp$ Linear configuration. The polarization changes between circular and linear periodically. Drawing by Alexander Mück [9].

1.4 Polarization Gradient Cooling

Experimental measurements of temperatures below the Doppler limit called for new models. In particular, we briefly summarize polarization gradient cooling for Linear $\perp$ Linear and $\sigma^+ - \sigma^-$ configurations as described by Dalibard and Cohen-Tannoudji [8]

1.4.1 Polarization Gradient field: Linear $\perp$ Linear

Consider the situation of a pair of counterpropagating laser beams with perpendicular linear polarizations (say $\hat{\boldsymbol{\varepsilon}}_{\text{left}} = \hat{\mathbf{x}}$ and $\hat{\boldsymbol{\varepsilon}}_{\text{right}} = \hat{\mathbf{y}}$). The total field is the sum

$$
\begin{aligned}
\mathbf{E}/E_0 &= \hat{\mathbf{x}} \cos(\omega_{\text{laser}} t - kz) + \hat{\mathbf{y}} \cos(\omega_{\text{laser}} t + kz) \\
&= (\hat{\mathbf{x}} + \hat{\mathbf{y}}) \cos(\omega_{\text{laser}} t) \cos(kz) + (\hat{\mathbf{x}} - \hat{\mathbf{y}}) \sin(\omega_{\text{laser}} t) \sin(kz).
\end{aligned}
\tag{1.17}
$$

This field is shown in Figure 1.3. The field at some locations of interest is given by:

$$
\mathbf{E}(z = 0)/E_0 = (\hat{\mathbf{x}} + \hat{\mathbf{y}}) \cos(\omega_{\text{laser}} t)
\tag{1.18}
$$

corresponding to linear polarization at 45º, similarly at $z = \lambda/4$ the field is linear at -45º. Another interesting location is at $z = \lambda/8$; the field there is

$$\mathbf{E}(z = \lambda/8)/E_0 = \hat{\mathbf{x}} \sin(\omega_{\text{laser}} t + \pi/4) - \hat{\mathbf{y}} \cos(\omega_{\text{laser}} t + \pi/4). \qquad (1.19)$$

This is circular polarization (σ^-), similarly at $z = 3\lambda/8$ the field is circular with the opposite helicity (σ^+) [5].

1.4.2 Sisyphus Cooling

One model for sub-Doppler cooling is that of linear $\perp$ linear polarization gradient cooling — so-called Sisyphus cooling (Dalibard and Cohen-Tannoudji considered a $J = {}^1/_2 \rightarrow {}^3/_2$ transition, as we will discuss here). The polarization gradient field as discussed in the previous section has important effects.

In addition to driving level transitions, the interaction of light with an atom may cause so-called 'light shifts'. This can be thought of as a Stark effect, of sorts, with the electric field of the light. It is important to note that these are not the same for various sublevels — different polarizations can produce very different light shifts. Figure 1.4 shows the position dependence of the light shifts of the ground-state sublevels. At the location of σ^- (see Figure 1.3), optical pumping drives the ground state population towards the $M_g = -{}^1/_2$ sublevel. For σ^+, the population is driven towards the $M_g = +{}^1/_2$ sublevel. Looking at Figure 1.4 one can imagine this cooling process. As an atom moves through space, it climbs the potential hill — that is, kinetic energy is converted into potential energy. Before sliding down the other side of the hill, the atom may be optically pumped to the other ground state sublevel. In
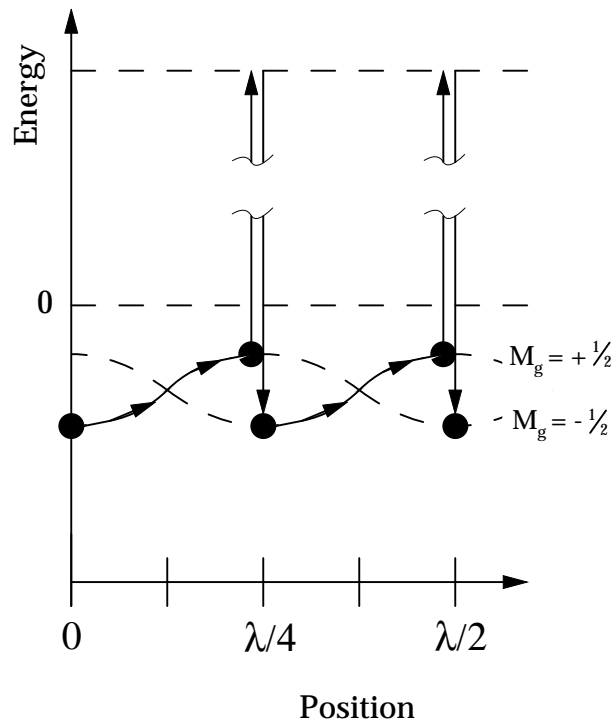
Figure 1.4: Position dependence of the light shifts of the ground-state sublevels and optical pumping. Based on a drawing by Alexander Mück [9].

the optical pumping process here, the spontaneously emitted photon is slightly higher energy then the absorbed photon. So the some of the atom's kinetic energy is radiated away.

1.4.3 Polarization Gradient field: $\sigma^+ - \sigma^-$

Now consider counterpropagating laser beams with circular polarization of opposite helicity (say σ^+ from the left and σ^- from the right). The total field

is the sum

$$\mathbf{E}/E_0 = [\hat{\mathbf{x}}\cos(\omega_{\text{laser}}t - kz) + \hat{\mathbf{y}}\cos(\omega_{\text{laser}}t - kz)]$$

$$+ [\hat{\mathbf{x}}\cos(\omega_{\text{laser}}t + kz) - \hat{\mathbf{y}}\cos(\omega_{\text{laser}}t + kz)] \qquad (1.20)$$

$$= \cos(\omega_{\text{laser}}t)[\hat{\mathbf{x}}\cos(kz) + \hat{\mathbf{y}}\sin(kz)].$$

This is a linear polarization that rotates along the z-axis as shown in Figure 1.5.
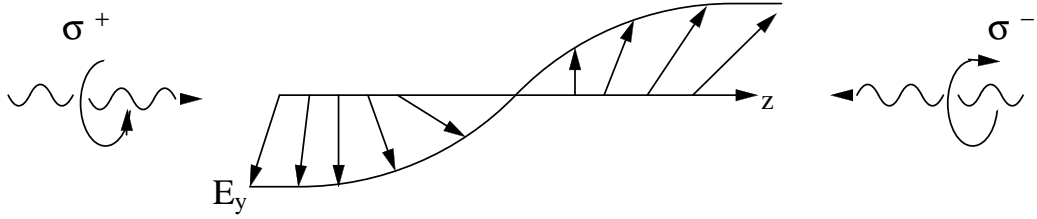
Figure 1.5: Polarization gradient in $\sigma^+ - \sigma^-$ configuration. The polarization is linear and rotates in space. Drawing by Alexander Mück [9].

1.4.4 $\sigma^+ - \sigma^-$ Polarization Gradient Cooling

Another model for sub-Doppler cooling introduced by Dalibard and Cohen-Tannoudji is for the $\sigma^+ - \sigma^-$ configuration (they assumed $J_g = 1$). As discussed in the previous section, the polarization is linear and rotating. Obviously in the $\sigma^+ - \sigma^-$ case, Sisyphus cooling is not possible since the polarization is linear everywhere (i.e., the light shift is uniform). An atom in this field sees a rotating axis of quantization. The population of the ground state must be optically pumped to follow. This pushes ground population towards the $M_g = +1$ sublevel and towards the $M_g = -1$ sublevel when the atom is moving toward the σ^+ and the σ^-, respectively. An atom with population in the

$M_g = +1$ state will scatter σ^+ light more efficiently (according to the Clebsch-Gordan coefficients), and vice versa. So an atom moving towards either beam will experience a damping force. Although it has a similar apparent effect to that of Doppler cooling, this is purely due to differential scattering of light, and not caused by the Doppler shift as discussed in Section 1.2.

1.5 Low Velocity Intense Source of Atoms

The idea of this project is to create a convenient tool to quickly load large numbers of sodium atoms in a magnetic trap for evaporative cooling to be used in experiments of fundamental quantum mechanics. Here, we discuss the various possible configurations of such a source; the terminology of Diekmann *et al.* is used (e.g. 2D-MOT, LVIS, 2D$^+$-MOT) [1].

1.5.1 2D-MOT

In Section 1.3.1, we described a simple picture of a MOT in one dimension. One now imagines this extended to two dimensions in the lab. A Ioffe coil configuration (to be described in Section 2.2), produces a linear field gradient near the center of the trap in x and y and no gradient in z. The magnetic field zero defines a natural axis (the z-axis). One might direct red detuned laser beams of the correct polarization along the x and y-axes. Atoms from the vapor are then pushed towards the z-axis and cooled, but their velocity component in the z direction is preserved. Therefore, it is expected such a configuration will produce atomic beams in both directions along the axis of the zero field (z-axis). This is shown pictorially in Figure 1.6. In order to limit the velocity of atoms in an atomic beam, one may put a small aperture
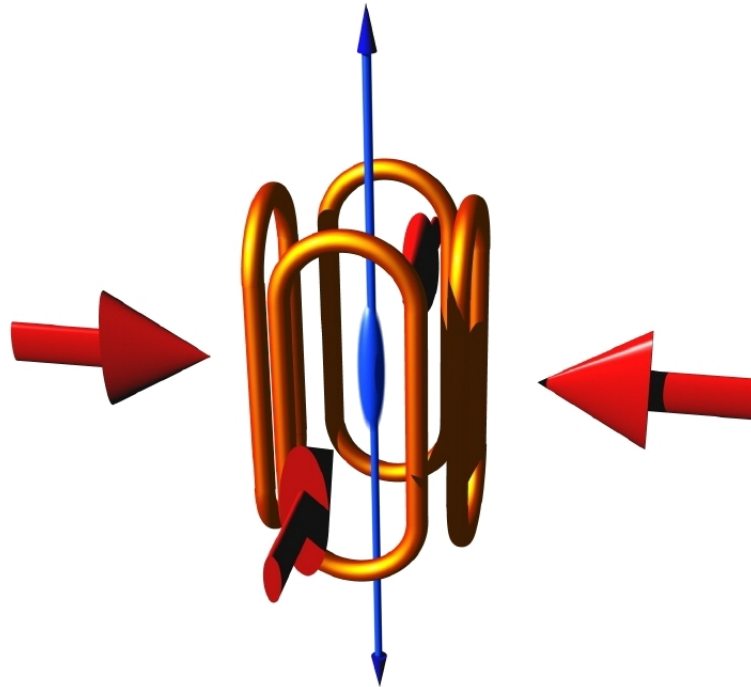
Figure 1.6: 2D-MOT pictorial. The Ioffe coils produce a linear magnetic field gradient in two dimensions. The axis of zero field is the atomic beam axis. Atomic velocity along this axis is preserved. Drawing by Todd Meyrath with Windell Oskay.

for the atomic beam to pass through. Atoms with large velocity components in the z direction do not spend enough time in the transverse cooling region to keep them from being filtered by the aperture downstream. Therefore, the atomic beam has mean velocity much smaller than that of the background atoms. Dieckmann *et al.* did this experiment with an elliptical beam size of $w_z = 24\,\text{mm}$ and $w_\rho = 7\,\text{mm}$ major and minor waists, respectively. The purpose of the elongated laser beams along the atomic beam axis is to have as large a trapping region as possible. The results obtained by Dieckmann *et al.* for this setup include a significantly larger mean velocity and width of

velocity distribution (see Figure 2 in reference [1]) than the LVIS and $2D^+$-MOT configurations to be described in the next two sections.

1.5.2   LVIS

LVIS is an acronym that stands for Low Velocity Intense Source [2]. Dieckmann *et al.* use 'LVIS' to refer to a specific type of configuration (other then the 2D-MOT or $2D^+$-MOT), although "Low Velocity Intense Source" should, in principle, refer to any configuration that has such characteristics (such as the 2D-MOT or $2D^+$-MOT). Instead of the Ioffe configuration of the 2D-MOT, the LVIS is similar to a standard MOT with the anti-Helmholtz coil configuration (as in Figure 1.2). It differs by having a shadow region in one beam. A common experimental setup involves retroreflecting the beams — one group designing an LVIS used a gold coated quarter wave plate with a small drilled hole as a retroreflecter [3]. The quarter wave plate is for the polarization and the coating for reflection, i.e. the beam passes through the quarter wave plate before and after reflecting from the back side. Diekmann *et al.* used an aluminum mirror at 45° with a small hole drilled in it as a reflector of a separately controlled beam. In the LVIS configuration, atoms experience unbalanced radiation pressure and escape as an atomic beam through the hole.

1.5.3 $2D^+$-MOT

Diekmann *et al.* performed three experiments in the same apparatus, the third of which they called the $2D^+$-MOT. This design might be considered similar to both the 2D-MOT and LVIS of the previous sections. The basic setup is the same as the 2D-MOT, but with an added pair of laser beams along the
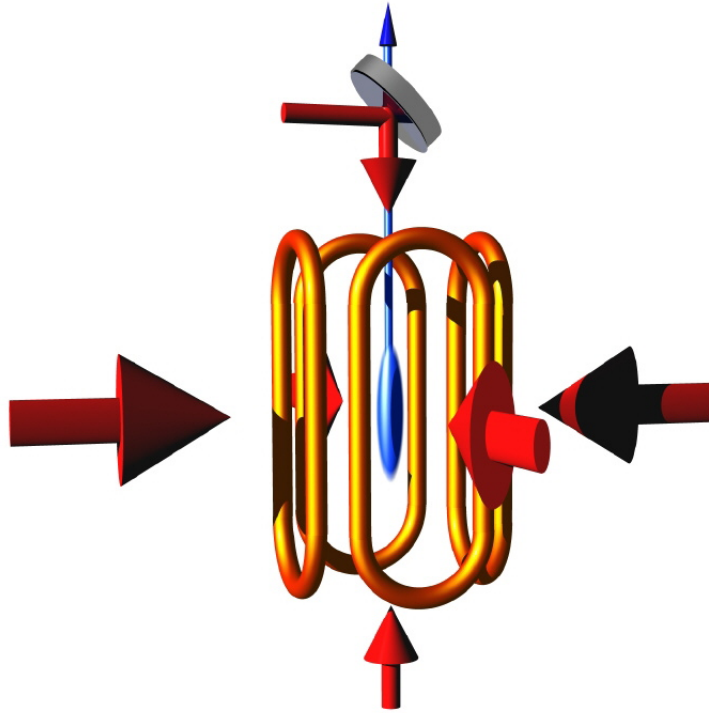
Figure 1.7: 2D$^+$-MOT pictorial of the Diekmann *et al.* setup. The Ioffe coils produce a linear magnetic field gradient in two dimensions. The axis of zero field is the atomic beam axis. Beam passes through the hole in an aluminum mirror. Drawing by Todd Meyrath with Windell Oskay.

atomic beam axis (hence the plus sign in the name). Similar to their LVIS setup, they used an aluminum mirror at 45º with a small hole drilled in it (see pictorial in Figure 1.7). This mirror acts as an aperture and to provide a situation of unbalanced radiation pressure. The lasers along the atomic beam axis are optical molasses beams. They provide cooling in that direction in addition to the transverse cooling of the MOT beams. The result obtained by Diekmann *et al.* are significantly lower mean velocity and width of velocity distribution. Comparing the LVIS and the 2D$^+$-MOT, the mean velocities are 26 m/s and 8 m/s with FWHM of 6.3 m/s and 3.3 m/s, respectively (see Figure

2 in reference [1]). Diekmann *et al.* obtained an atomic flux of order $10^{10}\,\text{s}^{-1}$. These numbers were inspiration to build a 2D$^+$-MOT — this project.

1.6   Sodium

1.6.1   Very Brief History and General Properties

General Na characteristics		
atomic number	Z	11
total nucleons	$Z + N$	23
nuclear spin	I	3/2
atomic mass	m	22.9898 u
		($3.8175 \times 10^{-26}\,\text{kg}$)
density at 25ºC	$\rho(25^\text{o}\text{C})$	$0.97\,\text{g/cm}^3$
vapor pressure at 25ºC	$P_\text{V}(25^\text{o}\text{C})$	$2.2 \times 10^{-11}\,\text{torr}$
vapor pressure at 100ºC	$P_\text{V}(100^\text{o}\text{C})$	$1.3 \times 10^{-7}\,\text{torr}$
vapor pressure at 150ºC	$P_\text{V}(150^\text{o}\text{C})$	$7.1 \times 10^{-6}\,\text{torr}$
melting point	T_M	$97.8\,^\text{o}\text{C}$
boiling point	T_B	$883\,^\text{o}\text{C}$
ground-state configuration		$1s^2 2s^2 2p^6 3s$

Table 1.1: General properties of sodium [10, 11].

In 1807, using electrolysis of caustic soda, Davy isolated the first elemental sodium. Sodium is the sixth most abundant element on earth (about 2.6% of the earth's crust) and the most abundant alkali metal [11]. In elemental form, sodium is a soft, silvery metal. Sodium metal is very reactive (especially with water) and must be handled with care. Sodium in this experiment is contained in a sealed, evacuated glass ampoule. The ampoule is only broken under vacuum. Some general properties of sodium appear in Table 1.1.

Since in this experiment we are dealing with a vapor cell MOT, we are concerned with the vapor pressure of sodium. A plot of the vapor pres-
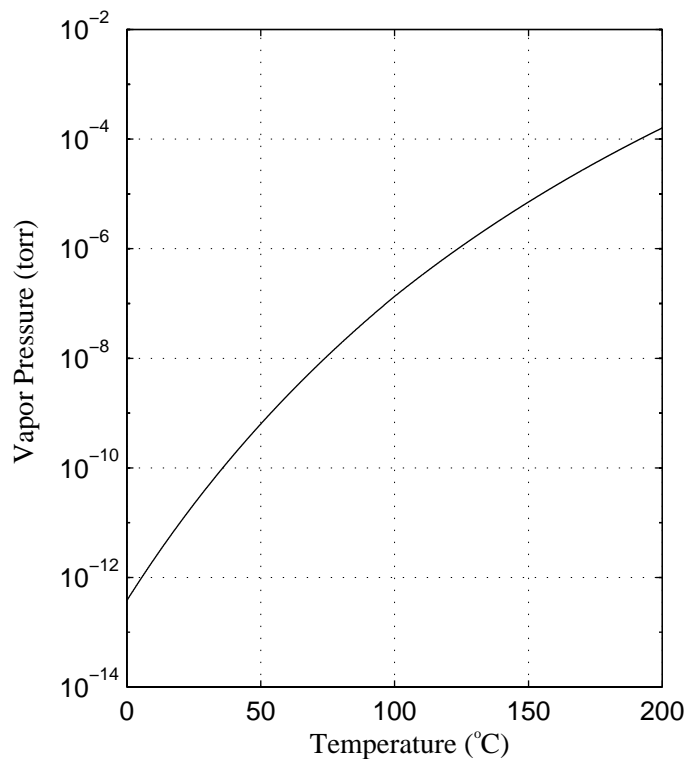
Figure 1.8: Sodium vapor pressure as a function of temperature [10].

sure appears in Figure 1.8. Obviously, the vapor pressure is too low at room temperature, therefore, we must heat it to over 100 °C.

1.6.2 Structure of Sodium

The ground state of sodium is $1s^2 2s^2 2p^6 3s$. The inner core electrons, $1s^2 2s^2 2p^6$, make up a closed shell and hence do not contribute to the orbital angular momentum of the atom. A contribution is only made by the $3s$ valence electron which has orbital angular momentum l and spin angular momentum s. Atomic momenta are then $\mathbf{L} = \mathbf{l}$ and $\mathbf{S} = \mathbf{s}$. Total angular momentum of the electron,

Na $3^2S_{1/2} - 3^2P_{3/2}$ transition characteristics		
frequency	ν	$5.0885 \times 10^{14}\,\mathrm{Hz}$
wavelength (vacuum)	λ	$589.158\,\mathrm{nm}$
lifetime of upper state	τ	$16.269\,\mathrm{ns}$
linewidth	$\gamma/2\pi$	$9.795\,\mathrm{MHz}$
saturation intensity	$I_\mathrm{s} = \frac{\pi h c}{3\lambda^3 \tau}$	$6.26\,\mathrm{mW/cm^2}$
recoil velocity	v_r	$2.945\,\mathrm{cm/s}$
recoil energy	E_r	$h \times 25.00\,\mathrm{kHz}$
Doppler limit	T_D	$240.18\,\mu\mathrm{K}$

Table 1.2: Characteristics of sodium $3^2S_{1/2} - 3^2P_{3/2}$ transition [5, 10, 11].

J, has well known values

$$|L - S| \leq J \leq L + S. \tag{1.21}$$

The L-S coupling energy, $V_{\mathrm{L-S}}$, is dependent on the orientation of **L** and **S**, i.e. $V_{\mathrm{L-S}} \sim \mathbf{L} \cdot \mathbf{S}$. This causes splitting of the principle levels and is called the fine structure. In standard notation, the ground state is $3^2\mathrm{S}_{1/2}$ and the first excited states are $3^2\mathrm{P}_{1/2}$ and $3^2\mathrm{P}_{3/2}$.

Further structure, called the hyperfine structure, can be understood by considering the coupling of the electron total angular momenta **J** with the nuclear spin **I**. The coupling energy of the electron with the nuclear spin depends on the orientation, $V_{\mathrm{I-J}} \sim \mathbf{I} \cdot \mathbf{J}$. The total angular momentum is denoted $\mathbf{F} = \mathbf{L} + \mathbf{S} + \mathbf{I}$. Similar to Equation (1.21), the values F may take are

$$|I - J| \leq F \leq I + J. \tag{1.22}$$

In particular, for sodium, the value of the nuclear spin is $I = 3/2$. So, for the $3^2S_{1/2}$ ground state, we see that F may have values $F_g = 1$ and 2. For the $3^2P_{3/2}$ excited state, F may have values $F_e = 0, 1, 2$, and 3.

Each hyperfine level with some F has $2F + 1$ Zeeman sub-levels which are degenerate in the absence of external fields. In the presence of a weak external magnetic field $\mathbf{B}$, the degeneracy is lifted as levels are shifted by

$$E_{\text{Zeeman}} = g_F \mu_{\text{B}} M_F B, \qquad (1.23)$$

where g_F is the Landé g-factor, $\mu_{\text{B}} = e\hbar/2m_{\text{e}}c$ is the Bohr Magneton, M_F is the angular momentum projection along $\mathbf{B}$, and B is the magnitude of the external magnetic field [12]. This is called the Zeeman effect. The hyperfine
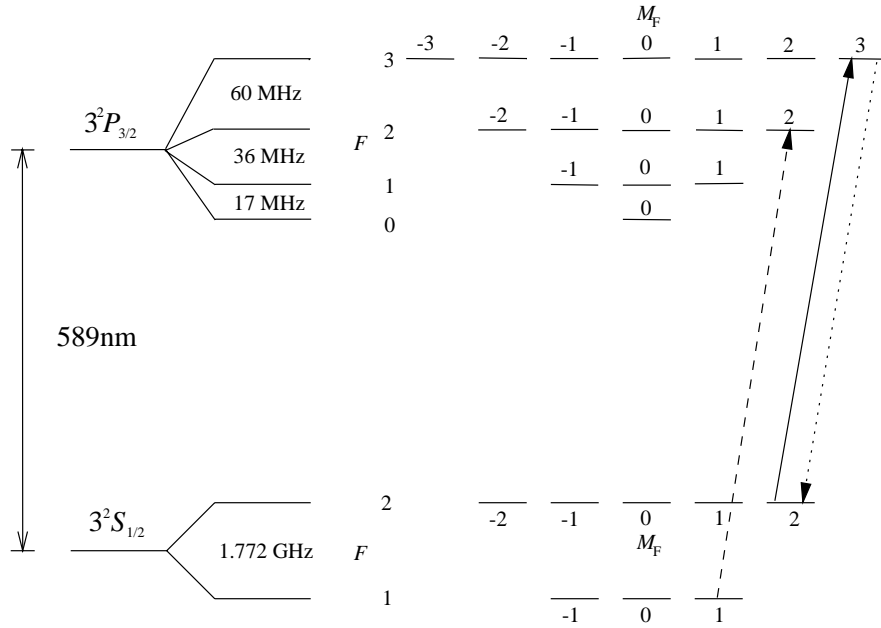
Figure 1.9: Sodium structure for the D_2 line. The stretched state transition (solid line and dotted line) and the repump (dashed line) are shown.

structure is shown in Figure 1.9 for the sodium D_2 line. The $3^2 S_{1/2} - 3^2 P_{3/2}$ transition, specifically, is used for cooling and trapping. Circular light couples the $|F_g = 2, M_g = 2\rangle$ and $|F_e = 3, M_e = 3\rangle$ states. In a MOT, with circular polarization of both helicity the atom could end up decaying to the $|F_g = 1\rangle$

ground state. Because of this, a repump laser is needed to return such atoms to the MOT transition. In this experiment, the required frequency shift of 1.77 GHz is provided by a combination of an acousto-optic modulator (AOM) and an electro-optic modulator (EOM). There are then two distinct beams: the MOT beam and the repump beam. These beams are provided by the lasers and modulators of the main sodium experiment.

Chapter 2

Experimental Design
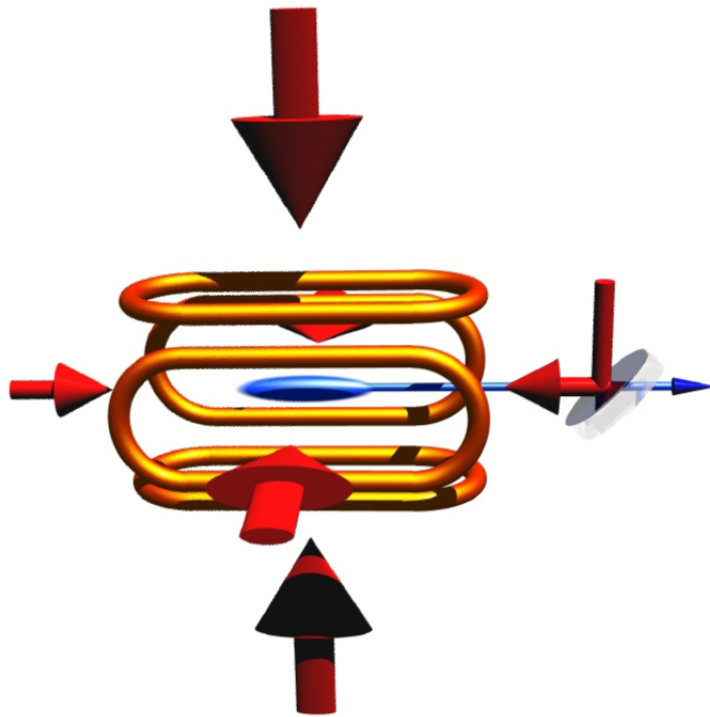
Figure 2.1: A pictorial of our chamber in operation. This is very similar to that of Dieckmann *et al.* as pictured in Figure 1.7. On the right is the 'LVIS mirror'. The four elliptical beams enter the sides of the glass cell (not shown) and the smaller circular beam (on the left) enter the end of the cell. Drawing by Todd Meyrath with Windell Oskay.

2.1   Chamber Design

2.1.1   The Idea

The setup for this experiment is similar in principle to that of the $2D^+$-MOT of Dieckmann *et al.* as described in Section 1.5.3. The cooling is done in a rectangular glass cell. Four large elliptical beams enter the cell on the sides — these are MOT beams. A smaller circular beam enters the cell on the end and another circular beam reflects off a special mirror and into the glass cell — these are optical molasses beams. The elliptical MOT beams contain repump light and the circular optical molasses beams do not. As discussed before, this leads to an atomic beam that exits the trapping region along the magnetic field axis. The setup is shown pictorially in Figure 2.1. The featured parts of the vacuum chamber are the 'LVIS mirror' and the glass cell.

2.1.2   The Mirror and Glass Cell

The LVIS mirror was fabricated for us by CVI Laser. It is a Zerodur ceramic glass elliptical mirror blank that has been drilled through with a diamond core-drill (see Figure 2.2). The hole is of several levels, narrow at the mirror surface (0.05 inch minor axis) and wide at the rear. This was done primarily so that the inside of the mirror would not prevent clearance through the hole in the case of somewhat imperfect orientation of the mirror. The mirror has a high reflectivity laser line coating at 589 nm. The primary reason we decided to have a dielectric coating rather than a protected silver coating is that the metal coating is a 'cold coating' and can not be baked (the chamber bake out is discussed in Section 2.1.4) to more than a modest 125 °C or so, but the dielectric coating is specified to be bakable to 300 °C. This is not necessarily a
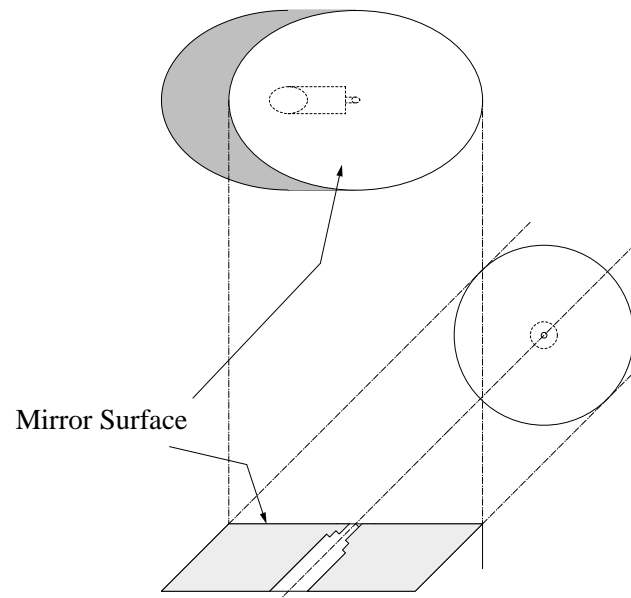
Mirror Surface

Figure 2.2: The LVIS mirror. The LVIS mirror is a Zerodur ceramic glass elliptical mirror blank that has been core-drilled and coated with a laser line dielectric coating at 589 nm. The hole at the mirror surface is elliptical with 0.05 inch minor axis. The mirror blank was cut out of a Zerodur rod at 45°.

concern in this test chamber, however, it could be when this setup is installed on the main chamber. One concern about this dielectric coating was that it might not preserve the phase difference in the s and p polarizations — which is necessary in order to reflect circular polarization without a change. Such a problem could potentially be fixed by making the incoming light of the correct elliptical polarization such that the reflected light would be circular. This is a phase correction, no amplitude difference correction would be needed since the mirror was a high reflector for all angles of linear polarization. We learned by testing the mirror prior to its placement in the chamber that it is insensitive to the polarization — it preserved the phase difference between the s and p light and therefore preserved circular polarization. However, after

the chamber bakeout procedure, we noticed that the mirror's properties had changed. The mirror became, in effect, a polarizing beam splitter. Because of this, we were forced to use a lin $\perp$ lin configuration (that is, the pair of beams with perpendicular linear polarization) for the optical molasses beams instead of circular polarizations. To be certain that we had not been in error when testing the mirror prior to the bake, we re-tested an identical mirror (that was coated in the same coating run as the mirror in the chamber) and found the same polarization insensitivity as previously observed.

In designing a mount for the mirror, several things had to be considered: the mirror was to be in the vacuum chamber (which must be baked) and is oddly shaped (see Figure 2.2). The mount, shown in Figure 2.3, was machined out of aluminum. The design is intended to naturally hold an elliptically shaped mirror. A pair of set screws provide two points of contact. The upper part of the mirror is pushed by three springs against a pin (a longer set screw) to provide a third contact point. The springs each sit in a blind hole. The bottom tip of the mirror sits on a small lip inside the holder. With the mirror in place and the screws adjusted, the mirror does not touch the inner rim of the holder. A small amount of pressure will not rock the mirror back and forth in its place but a more firm push can move it against the springs. When baking, the holder and screws expand and the springs provide the expansion space so that the mirror is not cracked. This holder is mounted on a reducer flange that has a hole in the center.

The cooling and trapping region is in a rectangular Pyrex cell. The dimensions of the cell are 1.5 inches by 1.5 inches on the end with a length of
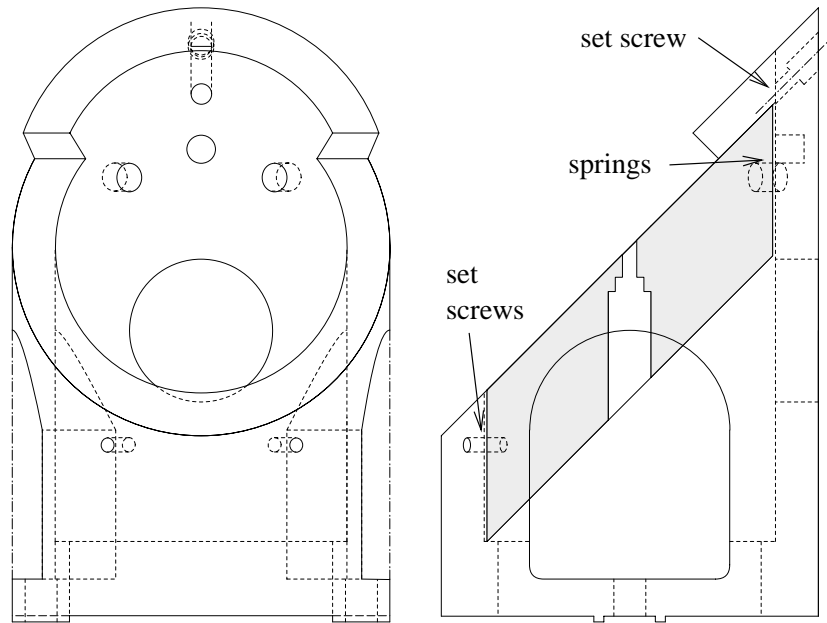
Figure 2.3: Aluminum mount that holds the elliptical mirror inside the chamber. The mirror is shown in place on the right. The elliptical mirror rests on the lower lip and is pushed by two steel set screws. Near the top of the mirror, three tungsten springs push the mirror against another steel screw that is at 45° to the vertical (i.e., parallel to the surface of the mirror). This holds the mirror firmly in place and provides expansion room during the bake to ensure that the glass mirror substrate is not cracked by the screws or holder.

4 inches. The rectangular glass cell is attached to a tubular glass to metal seal. The metal is welded to a standard conflat (CF) flange that is attached to the rest of the vacuum chamber. The use of a glass cell provides some advantages over steel chamber type configurations, in particular its compactness. With such a cell, we have large windows without the bulk of a large windowed steel piece. The compactness in particular allows magnetic coils to be relatively close to the trapping region inside the cell enabling high fields with relatively low current. Further discussion of the fields and currents are in Section 2.2.

Unfortunately, there are some problems with the cell. The specific cell that we have has very dirty windows — probably residue from the fabrication process. Some of the residue was cleaned off with solvents (including acetone and methanol) by wiping the inner and outer surfaces with lens tissue. Even after extensive cleaning, the windows still scatter much light due to the residue. Another problem of which we have become aware (from experiences with the main sodium experiment's Pyrex cell) is the fact that Pyrex windows tend to degrade in the presence of sodium. The degradation shows up in the form of greater scattering in the windows over time (and consequently loss of power from the beams) and possibly polarization changes. The exact effects are unclear as are the processes involved. However, we expect that replacing the Pyrex cell with a clean fused silica cell will improve the performance.

2.1.3 Vacuum Chamber Setup

The vacuum chamber includes the mirror and glass cell as discussed in the previous section along with other elements such as a valve and Varian StarCell ion pump. The chamber is shown in Figure 2.4. In the upper part of the chamber there is the glass cell that is attached to a custom steel cross. This custom piece has a small tube that goes to the pinch-off section that holds an ampoule of sodium. Opposite the glass cell, the custom cross has a zero length arm. The reducer flange to which the mirror holder is attached is connected at this location. It is rotated so that the mirror faces upwards through a window directly above it. A pair of windows face perpendicular to the plane of the paper in Figure 2.4a through which one can see the side of the mirror. These ports are to be used for a plug beam that will be discussed in Section 3.3.
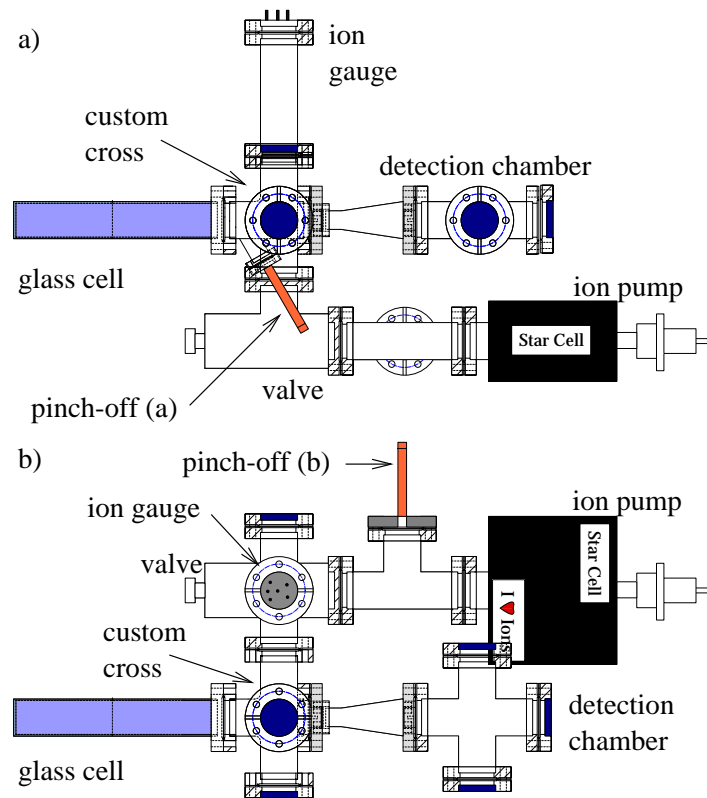
Figure 2.4: Chamber setup: a) side view: The glass cell is on the left. The pinch-off tube (a) contains the sodium. b) top view: The pinch-off tube (b) was used as the pump out port during bake out.

Beyond the reducer flange is a conical enlarger that attaches to the detection chamber. The detection chamber is a cross with three windows. The part of the optical molasses beam that passes through the hole in the LVIS mirror exits the facing window. A detection beam is passed through the pair of facing windows. Unfortunately, due to an oversight, we did not have another window to conveniently collect fluorescence. We, therefore, had to use the beam-splitter setup as discussed in Chapter 3. The remainder of the chamber consists of Bayard-Alpert type ion gauge to measure the pressure as well as

a Varian StarCell ion pump (discussed in Appendix A). A valve is located between the pump and the main part of the chamber that may be used to choke off the pump in order to allow for higher pressures in the chamber if that becomes desirable.

2.1.4   Chamber Bake

The reason for baking the vacuum chamber is to remove water, hydrocarbons, and other contaminants from the chamber walls. During this process, the chamber is connected to a portable vacuum pumping station (which we call the *turbo station*) through the pinch-off tube in Figure 2.4b. The station (designed by Dan Steck) consists of a mechanical roughing pump and a turbomolecular pump (discussed in Appendix A) that pump the chamber gas load during the bake. The station also has protection electronics to turn off the turbo pump in the event of a large leak or other such problem during the bake. We baked the vacuum chamber twice. The first bake was to approximately $300\,^{\circ}\mathrm{C}$ and the second to $225\,^{\circ}\mathrm{C}$. These temperatures are well within specifications for the parts. The first bake (without the glass cell or the Zerodur mirror), was primarily to make sure that the aluminum mirror holder was clean. The second, and final, bake was of the entire chamber. At the end of the second bake, the ion pump and the ion gauge were turned on briefly (flashed on). This was to clean them and allow the emitted particles to be removed from the system through the turbo pump. At that point in the process with the ion pump and the turbo pump running, the pressure in the chamber was 2.0×10^{-8} torr at room temperature. The chamber was then pinched-off from the turbo station to become an independent system. The process of pinching-

off is a simple. The copper tube is pinched by a special device. The device is consists of two very flat steel jaws that move parallel. The jaws squeeze the upper and lower halves of the copper tube together and the clean surfaces cold-weld. After pinching-off, the ion pump brought the chamber pressure down to 1.7×10^{-9} torr. The ion pump operates continuously thereafter.

2.2 Ioffe Fields

2.2.1 Field of an Infinite Line Current

The field of an infinite line current is well known [13] to have magnitude

$$|\mathbf{B}_{\text{line}}| = \frac{\mu_0 I}{2\pi r}, \tag{2.1}$$

where $r = \sqrt{x^2 + y^2}$ is the distance from the wire. In terms of a vector field we have

$$\mathbf{B}_{\text{line}}(x, y) = \frac{\mu_0 I}{2\pi} \left(\frac{-y}{x^2 + y^2} \hat{\mathbf{x}} + \frac{x}{x^2 + y^2} \hat{\mathbf{y}} \right), \tag{2.2}$$

where $\mathbf{I} = I\hat{\mathbf{z}}$ and $\hat{\mathbf{x}}$, $\hat{\mathbf{y}}$, and $\hat{\mathbf{z}}$ are perpendicular unit vectors.
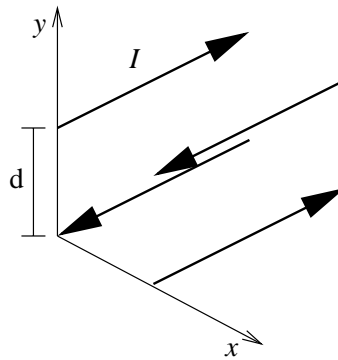
Figure 2.5: The ideal Ioffe configuration consists of four infinite equal line currents represented by the large arrows.
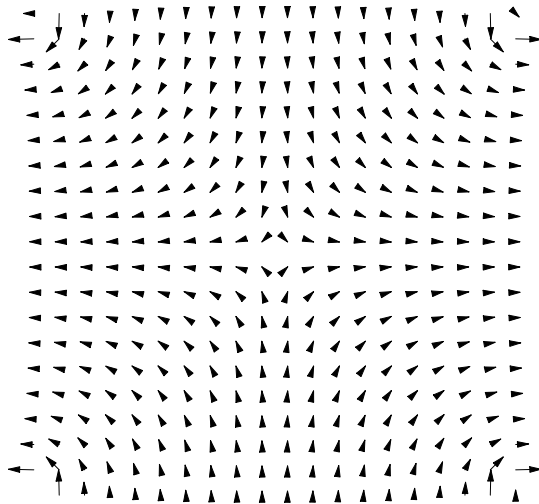
Figure 2.6: A vector field plot of $\mathbf{B}_{\text{Ioffe}}$ in the region between the four wires as in Equation (2.3).

2.2.2 Simple Calculations on Ideal Ioffe Configuration

The ideal Ioffe configuration consists of four infinite line currents of equal magnitude I and delta function thickness (see Figure 2.5). The resultant field is the vector sum of the single fields as in Equation 2.2:

$$
\begin{aligned}
\mathbf{B}_{\text{Ioffe}} = {} & \mathbf{B}_{\text{line}}(x - d/2, y - d/2) - \mathbf{B}_{\text{line}}(x - d/2, y + d/2) \\
& + \mathbf{B}_{\text{line}}(x + d/2, y + d/2) - \mathbf{B}_{\text{line}}(x + d/2, y - d/2).
\end{aligned}
\tag{2.3}
$$

A vector field plot of $\mathbf{B}_{\text{Ioffe}}$ is in Figure 2.6. Note, of course, that in this ideal case there is no z dependence and this solution can be translated along the z-axis. The magnitude, B_{Ioffe}, can be found to be

$$
\begin{aligned}
B_{\text{Ioffe}} &= \sqrt{\mathbf{B}_{\text{Ioffe}} \cdot \mathbf{B}_{\text{Ioffe}}} \\
&= \frac{4\mu_0 I}{\pi d^2} \sqrt{\frac{x^2 + y^2}{1 + \left(\frac{x^2 + y^2}{d^2}\right)^4 + 8\left(\frac{x^4 - 6x^2 y^2 + y^4}{d^4}\right)}}
\end{aligned}
\tag{2.4}
$$
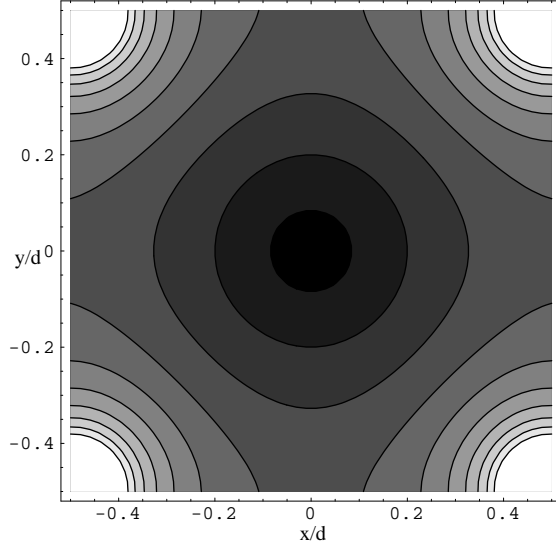
Figure 2.7: Contour plot of field magnitude in the region between the four wires as in Equation (2.4).

and is shown in Figure 2.7. Near the trap center (i.e., $|x|/d, |y|/d \ll 1$), we can approximate the second two terms in the denominator of the square root to be much less then one. Then we have an approximate linear dependent field magnitude given by

$$(B_{\text{Ioffe}})_0 \cong \frac{4\mu_0 I}{\pi d^2} r. \tag{2.5}$$

The approximate field gradient near the center of the trap is then

$$G_{\text{m}} \cong \frac{4\mu_0 I}{\pi d^2}, \tag{2.6}$$

as in Equation (1.9). This can be used to estimate the currents needed for particular field gradients or to determine the gradient produced by particular values of current.

The field gradient is important for MOT operation, but another factor to consider is alignment of the atomic beam axis to the hole in the mirror. By changing the relative currents in the Ioffe wires, one may shift the magnetic field axis. This of course will also skew the field from the straight line gradient above by a small amount which we will neglect. Consider Equation (2.3) at $y = 0$ with possibly different currents: I_n where $n = 1, 2, 3, 4$:

$$
\begin{aligned}
\mathbf{B}'_{\text{Ioffe}}(x, I_1, I_2, I_3, I_4) =&\, \mathbf{B}_{\text{line}}(x - d/2, -d/2, I_1 + I_4) \\
&- \mathbf{B}_{\text{line}}(x - d/2, +d/2, I_1 + I_2) \\
&+ \mathbf{B}_{\text{line}}(x + d/2, +d/2, I_2 + I_3) \\
&- \mathbf{B}_{\text{line}}(x + d/2, -d/2, I_3 + I_4),
\end{aligned}
\tag{2.7}
$$

where $\mathbf{B}_{\text{line}} = \mathbf{B}_{\text{line}}(x, y, I)$ as in Equation (2.2). Now, suppose we fix currents 2 through 4 and call them I_0 (i.e., $I_0 = I_2 = I_3 = I_4$) and vary I_1. We expect to see a shift in the zero of the field along the x axis. The position of zero field along the the x axis (call it x_0) is a solution to

$$
[\mathbf{B}'_{\text{Ioffe}}(x, I_1, I_0, I_0, I_0) \cdot \hat{\mathbf{x}}]_{x=x_0} = 0.
\tag{2.8}
$$

This equation can be solved with result:

$$
x_0^{\pm} = d \, \frac{-(I_1 + 3I_0) \pm \sqrt{-I_1^2 + 10I_1 I_0 + 7I_0^2}}{2(I_1 - I_0)},
\tag{2.9}
$$

where x_0^+ is the solution in the vicinity of the origin. This could also be written in terms of Δ_I defined by $I_1 \equiv I_0 + \Delta_I$:

$$
x_0^+ = d \, \frac{-(\Delta_I + 4I_0) + \sqrt{16I_0^2 + 8I_0 \Delta_I - \Delta_I^2}}{2\Delta_I}.
\tag{2.10}
$$

The formulas of this section can be used for practical estimates of the fields for some situations. A discussion about the actual design of the coils used to

produce these fields follows in Section 2.2.3. That discussion will make clear the choice of writing sums of currents in Equation (2.7). In Section 2.2.4 there is a discussion about actual measurements of the coils in operation and how they compare to this theory.

2.2.3   Ioffe Coils
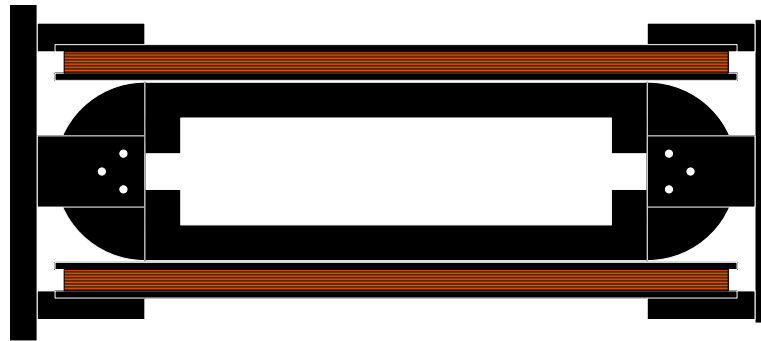
Figure 2.8: Side view of the assembled coil holders (note: assembly looks the same when looking normal to all four coils). The assembled coil holder consist of four racetrack shaped Delrin coils that are mounted on a circular aluminum holder that is then mounted to the vacuum chamber.

In order to approximate the ideal Ioffe configuration, we designed four racetrack shaped coils. The coil holders were machined out of Delrin — a hard plastic. They consist of several parts: the semi-disk end, rectangular end mount, and the long sides. The dimensions of each coil are 2.5 inches across in the short direction, 7 inches along the straight path on the sides, and half disk ends are of diameter 2.5 inches. The parts that make up each racetrack coil are held together by stainless steel screws and pins. The four coils are then mounted on a circular aluminum holder that is in turn mounted to the vacuum chamber. The end of the coil assembly is held together by a thin circular piece
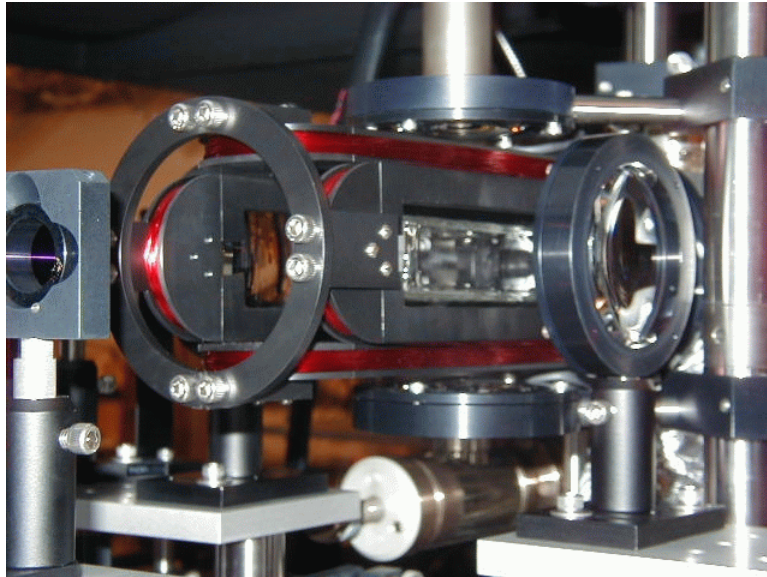
Figure 2.9: Photo of the coils in the setup. In the center one can see the glass cell surrounded by the black Delrin racetrack shaped Ioffe coils. They are wrapped with red magnetic wire. The coil assembly ends with a Delrin retaining ring for stability. Above and to the sides of the the coil assembly one can see the 3 inch lenses that are the objectives for the four large telescopes discussed in Section 2.4.1.

of Delrin. Figure 2.8 shows the side view of the assembly and Figure 2.9 is a photo of the coils in the optical table setup. The coil assembly is very strong, stable, and light weight. Gauge 24 magnet wire was wrapped around each of the four coils for 200 turns. The wire was wrapped in the counter clockwise direction (as looked on from the outer side when assembled) from white to grey connector wires. When hooked up to the current source electronics, care is taken so that each pair of adjacent wires has current in the same direction. Each of these pairs of 200 wires then makes up one of the Ioffe wires (hence why we wrote sums of currents in Equation (2.7)).

2.2.4 Field Measurements

We made measurements of the magnetic fields with a Bell Series 9350 Gauss-meter. The probe was mounted on an XYZ translation stage where the z axis could easily be found as the location where the x and y components of the field vanish and remain zero for a translation along the z axis. The measurements described here were made along the x axis with $y = 0$ (it is noted that measurements along the y axis produced similar results).

The first thing that we are interested in is the magnetic field gradient G_m as in Equation (1.9). The theoretical value of G_m is given by Equation (2.6):

$$G_\mathrm{m} = \frac{4\mu_0 I}{\pi d^2}. \tag{2.6}$$

We note that the formulas from Section 2.2.2 are for the ideal Ioffe case. That case is where the wires are infinitely long and are of negligible thickness. In the region of interest, these conditions are fairly well approximated. One point about the size of the wires is raised that they consist of 400 turns of small wire on two separate holders (i.e., the sides of two adjacent coils next to each other). In this approximation, it is not totally clear what value to use for d (the d in Figure 2.5) since the model assumes the wires are of negligible thickness. From the mechanical drawings a value of 60 mm to 70 mm is likely. For the purpose of estimation of current requirements for construction of electronics (Section 2.3), we used $d = 65$ mm. Field measurements were made along the x axis within a few millimeters of the zero field location. The results of these measurements for current $I = 0.5$ A and $I = 0.8$ A appear in Figure 2.10. The
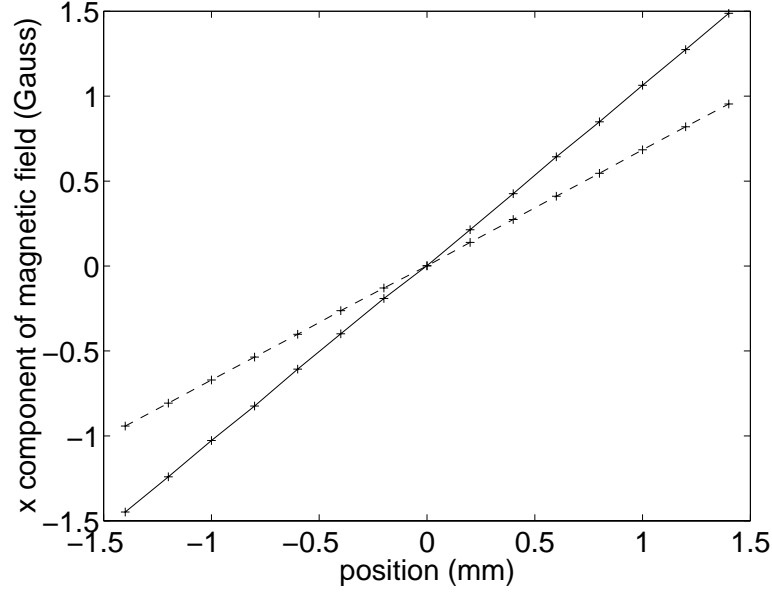
Figure 2.10: Measured magnetic field near center zero field line. This measurement was done in the x direction where the y and z components are zero. The dashed line is for current $I = 0.5\,\mathrm{A}$ in all coils. The solid line is for current $I = 0.8\,\mathrm{A}$ in all coils. The crosses mark the data points which have error less then $\pm 0.01\,\mathrm{G}$. It is noted that the sets of data form straight lines as expected from theory. The magnetic field gradients are $G_\mathrm{m}(I = 0.5\,\mathrm{A}) = 6.75\,\mathrm{G/cm}$ and $G_\mathrm{m}(I = 0.8\,\mathrm{A}) = 10.4\,\mathrm{G/cm}$, respectively.

measured values fit straight lines very well. From the measured values we can

determine G_m for the respective current, finding an average G_m as

$$\langle G_\mathrm{m} \rangle = \frac{1}{N} \sum_{n=1}^{N} \frac{B(x_n)}{x_n}, \tag{2.11}$$

where $\{(x_n, B(x_n))\}$ is the set of data points. Measurements give magnetic

field gradients of $\langle G_\mathrm{m} \rangle (I = 0.5\,\mathrm{A}) = 6.75\,\mathrm{G/cm}$ and $\langle G_\mathrm{m} \rangle (I = 0.8\,\mathrm{A}) = 10.4\,\mathrm{G/cm}$, respectively. If we assume Equation (2.6) is valid, then we can

determine d for those currents: $d(I = 0.5\,\mathrm{A}) = 68.8\,\mathrm{mm}$ and $d(I = 0.8\,\mathrm{A}) = 70.2\,\mathrm{mm}$ with average $\langle d \rangle = 69.5\,\mathrm{mm}$. If we use this as a reasonable estimate

Figure 2.11: This plot shows the change in the zero position of the magnetic field in the x direction for a change of current in coil 1. Coils 2 to 4 have current $I = 0.5\,\mathrm{A}$. The dotted line is for measured values and the solid line is theory (Equation (2.10) with $d = 69.5\,\mathrm{mm}$ and $I_0 = 0.5\,\mathrm{A}$).

of d and assume Equation (2.6) then we have

$$G_\mathrm{m} \cong \left(13.25 \, \frac{\mathrm{G}}{\mathrm{cm} \cdot \mathrm{A}} \right) I. \tag{2.12}$$

In addition to gradient measurements, we also considered the shift of the zero in the magnetic field along one axis for different currents. Plots of the results appear in Figure 2.11 and Figure 2.12 for different currents. Like the previous measurements, these were made along the x axis. The error bars for these measurements are much greater due to the lack of resolution on the current control electronics readout — which could potentially be improved. The plots, however, show reasonable agreement with the theory in Equation
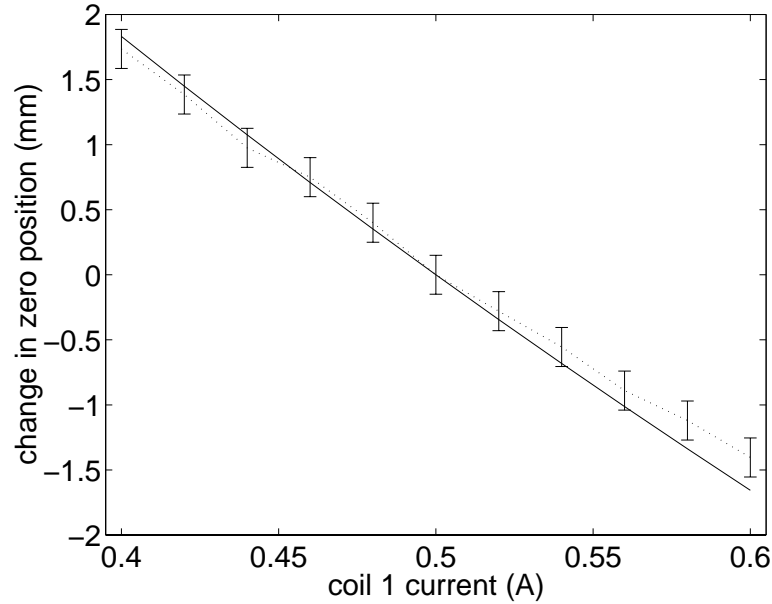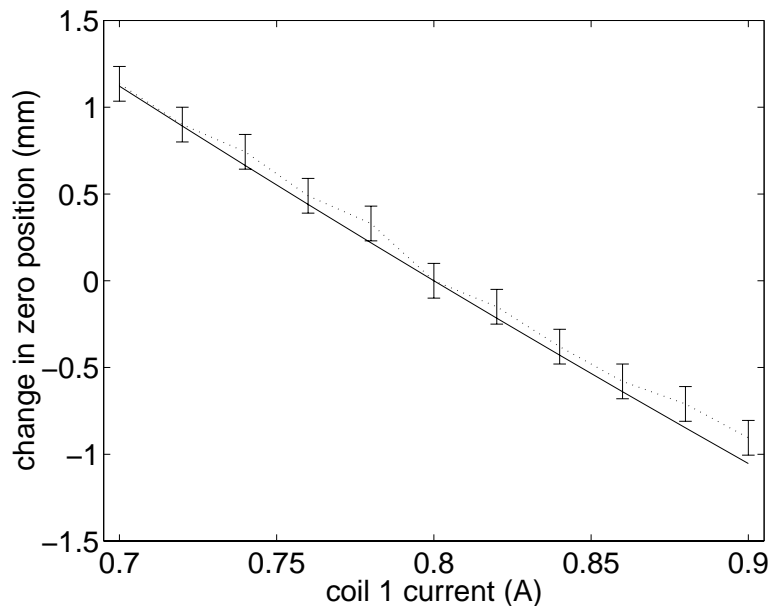
Figure 2.12: This plot shows the change in the zero position of the magnetic field in the x direction for a change of current in coil 1. Coils 2 to 4 have current $I = 0.8\,\mathrm{A}$. The dotted line is for measured values and the solid line is theory (Equation (2.10) with $d = 69.5\,\mathrm{mm}$ and $I_0 = 0.8\,\mathrm{A}$).

(2.10):

$$x_0^+ = d\,\frac{-(\Delta_I + 4I_0) + \sqrt{16I_0^2 + 8I_0\Delta_I - \Delta_I^2}}{2\Delta_I}. \qquad (2.10)$$

We can see that the zero position can be shifted by several millimeters for some $100\,\mathrm{mA}$ of current difference. Equation (2.10), using value $d = 69.5\,\mathrm{mm}$, can be used to estimate this shift.

2.3   Current Control Electronics

The purpose of these electronics is to provide a stable and independent current source for each of the four coils described in Section 2.2.3. Estimates of the current requirements for reasonable field gradients come from the coil design

and the theory of Section 2.2.2. The electronics described here can reliably supply well over 2 A of current to each coil. Of course, with currents over an Amp and a half or so overheating of the coils could be a problem. The electronics are also designed to provide a few options for control of these currents (i.e., interface options for the current box). The circuit consists of two parts: the power circuit and the control circuit. They will be described in this section [14, 15].

2.3.1 Power Circuit

Figure 2.13 shows the power circuit that drives the MOT coils. The key to the circuit is the IRF620. It is a power MOSFET by International Rectifier which can have up to 5.2 A of continuous drain current. It is a TO-220 type package and is attached to a heat sink with a thermo-pad for heat transfer and electrical isolation.

The part of the circuit that is in parallel with the coil is a type of "snubber" to suppress the inductive kick. This specific configuration was chosen because it gives a linear decay of the current in the coil. This is as opposed to a more typical configuration of a diode (such as the MR752 in Figure 2.13) with a resistor which would have a long exponential tail. For the circuit shown here in Figure 2.13, when the FET is suddenly turned off, we have

$$L\frac{\mathrm{d}I}{\mathrm{d}t} + V = 0, \tag{2.13}$$

where L is the inductance of the coil load and V is the sum of the other voltage drops (zener, transistor, and diode). So, we have

$$I(t) = I_0 - \frac{V}{L}t, \tag{2.14}$$
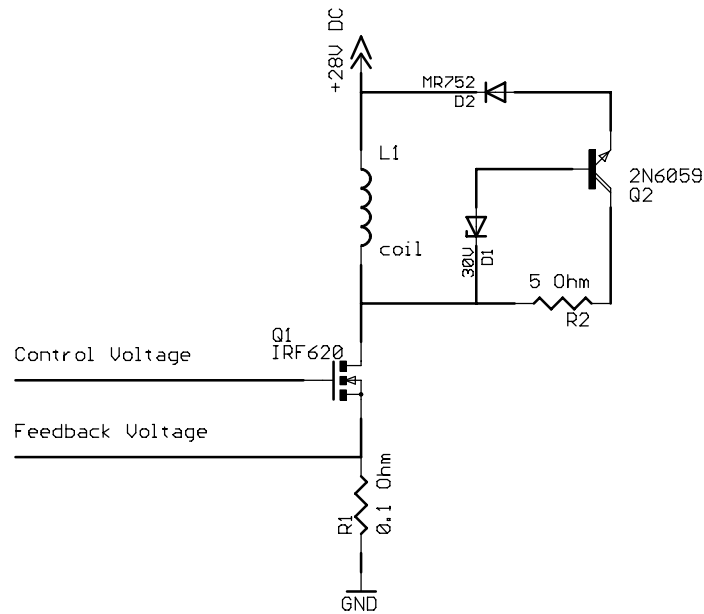
Figure 2.13: Power circuit. Current is controlled by the FET, the "snubber" part of the circuit is to limit the inductive kick and provide a fast shutoff of the field.

which, of course, is only the case when the transistor (2N6059) is turned on (i.e., when the voltage across the zener is the zener voltage). So, as the current is close to zero, it would not be surprising to see small oscillations in the field. This setup is useful in situations where fast turn off is important and could be potentially optimized for temporal requirements with a choice of the zener diode, transistor, etc. for the particular inductive load that is used. For application in this experiment, however, fast turn off is not needed since the coils are to be operated with constant current. The snubber is also needed, of course, to prevent inductive kick from destroying the electronics. All of the components of the power circuit are mounted on a large heat sink that is air cooled.

One point of caution when operating this circuit is that although the maximum current through the IRF620 is around $5\,\mathrm{A}$, the maximum power is $P_{\mathrm{max}} = 50\,\mathrm{W}$. The power supply voltage drops over the coils and the IRF620 (ignore the $0.1\,\Omega$ resistor). Therefore, the supply voltage, V_{supply}, should be chosen for the coil resistance, R_{coil}, and the circuit should operate with a current, I, that satisfies the inequality:

$$IV_{\mathrm{FET}} = I(V_{\mathrm{supply}} - R_{\mathrm{coil}}I) \leq 50\,\mathrm{W}. \tag{2.15}$$

In the case of our coils, with resistance of about $9.5\,\Omega$, we use a supply voltage of $+28\,\mathrm{V}$. In this case, the maximum power through the FET is about $20\,\mathrm{W}$ at about $I = 1.5\,\mathrm{A}$. With a $+28\,\mathrm{V}$ supply, the max current is a little less the $3\,\mathrm{A}$ — this is when there is no voltage drop across the FET (and the current is not regulated). So with this setup there is no concern that the FET will burn out. However, as the author learned the hard way, a smaller test load in place of the coils can easy cause burn out the FET. For example, with the $+28\,\mathrm{V}$ supply a minimum load of $5\,\Omega$ should be used to keep the maximum FET power at around $40\,\mathrm{W}$ (well below $P_{\mathrm{max}} = 50\,\mathrm{W}$).

2.3.2 Control Circuit

The control circuit is closely based on the design by Martin Fischer. It consists of a feedback loop with the voltage across the $0.1\,\Omega$ power resistor as a sense and the FET gate voltage as the control. The circuit is shown in Figure 2.14. There are several controls that can modulate the current, they are: front panel pot, external input, and TTL input. How this control circuit works can be understood by looking at a simplified general example as in Figure 2.15.
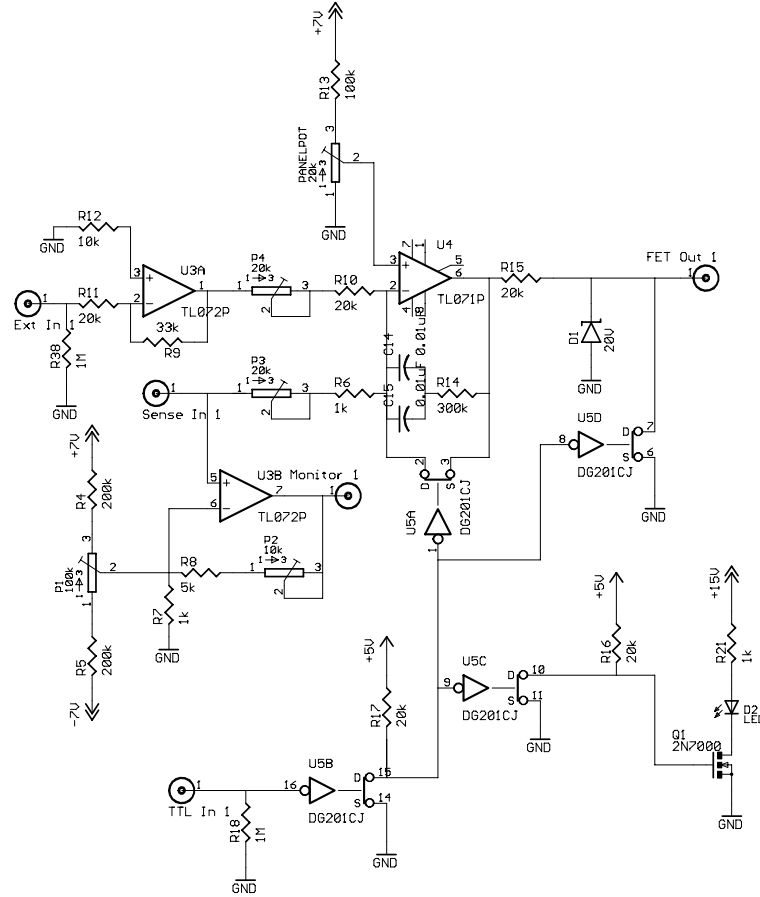
Figure 2.14: Current control circuit (based on design by Martin Fischer). Feedback loop with the power circuit controls the current in the coil.

Considering the case of the ideal opamp (i.e., infinite input impedance and equality of the input voltages), we can see that the output voltage is given by

$$V_O = \left(1 + \frac{Z_F}{Z_E} + \frac{Z_F}{Z_S}\right) V_P + \frac{Z_F}{Z_E} V_E - \frac{Z_F}{Z_S} V_S, \qquad (2.16)$$

where V_E (the external input) is negative because of the inverting amplifier UA3 in Figure 2.14. V_S is the voltage feedback sense. The output voltage (and hence the current since the the power FET gate is at this voltage) is
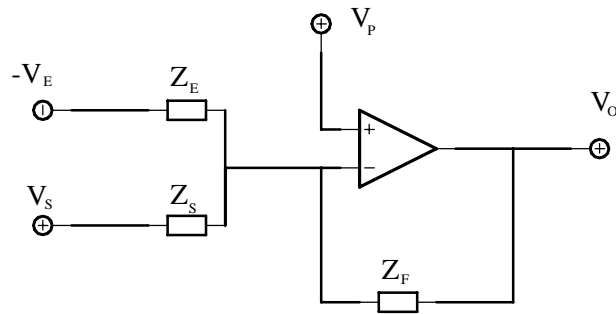
Figure 2.15: Simplified general example of the control circuit operation.

controlled by the external input and by the front panel pot (by setting V_P).

The TTL signal controls the analog switches DG201 in Figure 2.14. In this way, a high TTL signal is required to have current in the coils. One could, for instance, modulate the current by the TTL signal.
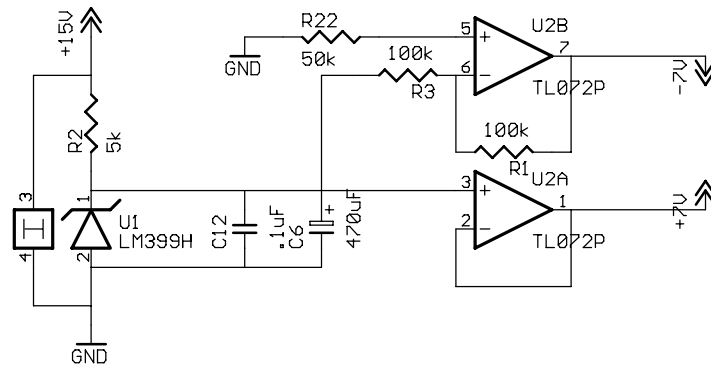
Figure 2.16: Stable voltage reference for control circuit in Figure 2.14. The LM399 package is a temperature stabilized zener diode which serves as the reference voltage of about 7 V.

A high precision voltage reference (LM399) is used for the important pots in the circuit. The LM399 package is a temperature stabilized zener diode

which serves as the reference voltage of about 7 V.

The control circuit and the voltage reference circuit for each channel were put on an etched copper circuit board. Discussion and drawings of these boards are in Appendix B.

Monitors of the current are a BNC front panel output and a LCD package. The LCD package is the DP-654 from Keithley Instruments. It is a convenient device which is essentially a voltmeter. It has a built-in A/D converter and a liquid crystal display. A small board is mounted on the LCD to serve the simple purpose of supplying the correct voltage to the LCD package from the voltage rails in the box. A photo of the box is shown in Figure B.1 in Appendix B.

2.4   Optical Setup

2.4.1   Large Elliptical Beam Concerns

Since, in this setup, we require large elliptical beams (about 48 mm waist diameter major axis and 16 mm minor), we require large optics for beam expanding telescopes. From the cost perspective, large cylindrical lenses are impractical, so we decided to use an anamorphic prism pair to make the beam elliptical when it is small and use a spherical telescope. The anamorphic prism pair is a convenient package that expands the beam $3\times$ in one direction only. Since the final beam size (major axis) is around 2 inch waist, we decided to use 3 inch objectives to avoid fringes as the result of beam clipping.

Another important feature of the beams is the circular polarization. Normally, in a situation with small beams, one keeps linear polarization until

right before entering the MOT chamber so that the quarter-wave plate is the last optic. That way one avoids polarization problems due to birefringence in dielectric mirrors, etc. The problem here, again, is the size of the beams — the cost of a 3 inch quarter-wave plate is painful to talk about, especially when 4 would be needed. Our solution to this problem is to use a small quarter wave plate and place it near the focus of the telescope. There the wavefront most resembles a plane wave. In this setup the objective of the telescope is then the final optic.

2.4.2 Laser and Practical Table Setup Concerns

Since this experiment is running in parallel with the main experiment (to which it is intended to become part), optical table space is limited. Using a different table is unrealistic because of the need for the dye-laser setup complete with frequency locking and modulators. So we built a level over the present optics. This simply consists of a large aluminum plate supported by stainless steel posts. Large holes in the plate were cut to allow MOT beam and repump beam to be periscoped up to the second level. On the main level, the lower periscope mirrors are placed on kinematic mounts so that they could be removed and replaced very easily. The optics for the horizontal beams are put on three very small third levels. Vertical optics are mounted on large steel posts.

2.4.3 Optical Setup

Most of the horizontal optical setup is shown in Figure 2.17. Two beams are brought up from the table below: the MOT beam and the repump beam. The MOT beam is linearly polarized (normal to the plane of the paper initially).

The upper periscope mirrors are labeled in Figure 2.17. The MOT beam passes through a $^1/_2$–wave plate and then through a polarizing beamsplitter cube. The $^1/_2$–wave plate is used to select the intensity balance between the large elliptical beams (the light that passes through the cube) and the small circular beams (the light that reflects from the cube). The light that reflects from the cube goes through a telescope to a final size of approximately 8 mm waist and then is split. Half the light is directed into the end of the glass cell and the other half is brought down onto the LVIS mirror and reflected into the cell. The MOT light that passes through the cube then enters another cube where it is combined with the repump light. A small amount of the MOT/repump light is taken by a beamsplitter to be used for the detection beams. The bulk of the MOT/repump light passes to an anamorphic prism pair where it is expanded $3\times$ in one direction. This small elliptical beam of MOT/repump light is split at a beamsplitter (located at the end of the coils in Figure 2.17). One half goes to the vertical telescopes (not shown), the other goes to the horizontal telescopes.

The major focus in the optical setup revolves around the glass cell and the beams that enter it. In Section 2.4.1 we discussed some of the concerns of the large elliptical beams. Because space is limited, especially in the vertical direction, we choose fast lenses in order to have the telescopes as short as possible. On one side, the small fast lens in conjunction with the large lens make a telescope. On the retroreflected side, a mirror is placed at the focus of the large lens to make a unity magnification telescope. Mounting of the pair of vertical telescopes (one above and one below the glass cell) was done using 90º post clamps to large steel posts (this is not shown in Figure 2.17). The

vertical and horizontal telescope setups are the same. Near the focus of each of the telescopes for the elliptical beams is a $^1/_4$–wave plate positioned to give the correct circular polarization.
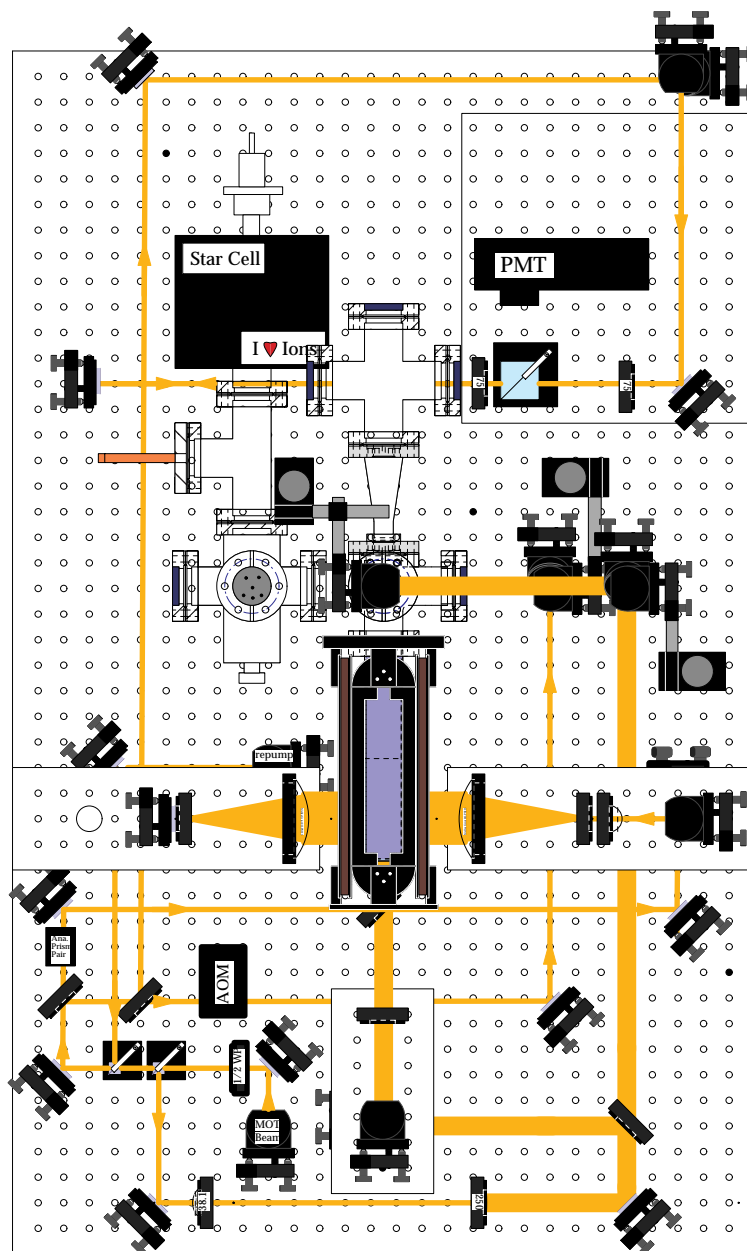
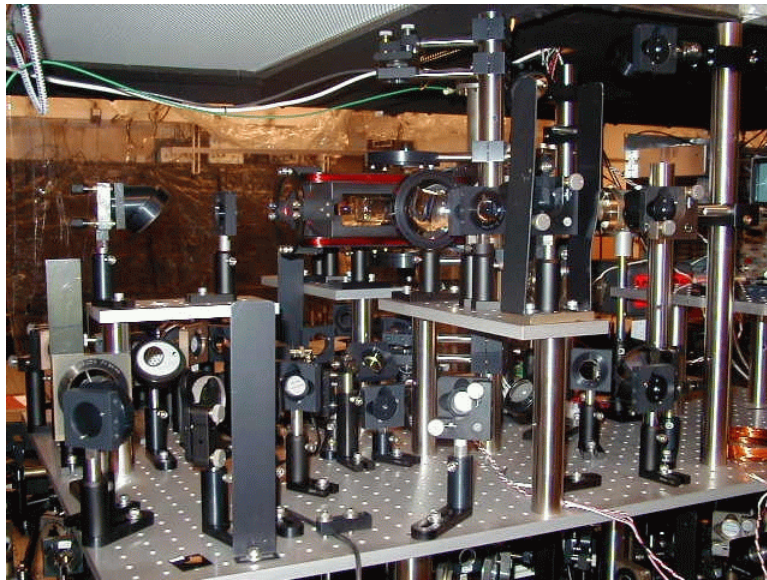Figure 2.17: Optics setup. See Section 2.4.3 for discussion.

Figure 2.18: Photo of optical setup. This is a photograph of the experiment at some mid-point of the setup.

Chapter 3

Detection, Observations, Conclusions

3.1   Detection Estimates

In an optimized setup, we might hope for atomic flux on the order of $10^8 \, \text{s}^{-1}$ (experiments of other groups [1, 2, 3] had similar or larger fluxs). Suppose the atoms are moving in a beam with velocity $10 \, \text{m/s}$. With a $1 \, \text{cm}$ detection beam of resonant light above saturation intensity there would be fluorescence of order $1 \, \mu\text{W}$ is all directions. Of course, in order for the setup to be optimized we need to be able to detect the atomic flux and maximize it by adjusting the magnetic field axis and the molasses beams. Therefore, initially, we are required to detect much weaker intensity. Furthermore, we are only able to collect some fraction of the fluorescent light onto a detector. More realistically, we are required to be able to detect light on the order of $1 \, \text{nW}$. This light level is difficult to see by eye and impossible for a photodiode, so we use a photo-multiplier tube (PMT).

One problem with our setup is the oversight in the construction of the chamber where a window to be used exclusively for the PMT was not included. Therefore, we were forced to setup the detection using a beamsplitter cube as shown in the upper right hand corner of Figure 2.17. This is problematic. In

addition to losing fluorescence intensity through the beamsplitter cube, the back-reflection of the detection beam must be blocked in order to prevent saturation of the very sensitive PMT. This can result in a very small signal above a large background.

In order to detect the atomic beam, we employ a lock-in technique. This is discussed in Section 3.3. First, we discuss the basics of lock-in amplifiers.

3.2 Lock-in Amplifiers

A lock-in amplifier can be used to detect small AC signals that may be obscured by noise several orders of magnitude larger than the signal. The lock-in can be thought of as behaving as a bandpass filter of very narrow bandwidth. The filter is centered at the frequency of the signal and rejects noise at all other frequencies.
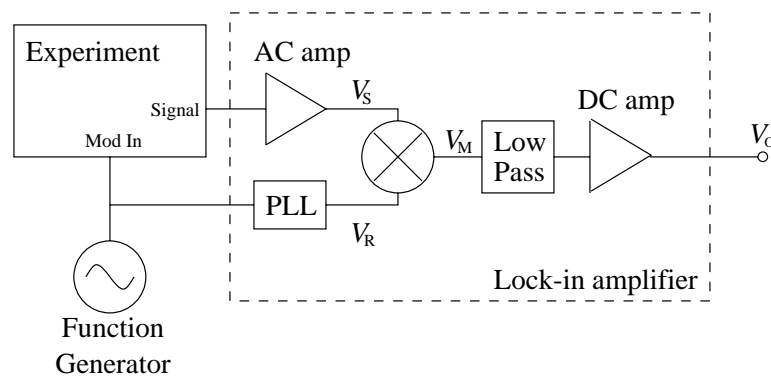

Figure 3.1: Lock-in amplifier block diagram.

For more details on the operation of a lock-in amplifier, we look at the block diagram in Figure 3.1. We have an experiment with some property that we can modulate and measure the response. A modulation signal is sent to

the experiment and to the lock-in as the reference. The experimental signal is the input to the lock-in: $V_S = A_S \cos(\omega_S t + \phi_S)$, where ϕ_S might be phase delay response of the experiment. The modulation signal is put into a phase locked loop (PLL) in order to generate a noise-free sinusoid $V_R = A_R \cos(\omega_R t + \phi_R)$ with adjustable phase ϕ_R. These two signals are then mixed with result:

$$
\begin{aligned}
V_M &= A_R A_S \cos(\omega_R t + \phi_R) \cos(\omega_S t + \phi_S) \\
&= \frac{1}{2} A_R A_S (\cos[(\omega_R + \omega_S)t + (\phi_R + \phi_S)] \\
&\quad + \cos[(\omega_R - \omega_S)t + (\phi_R - \phi_S)]).
\end{aligned}
\tag{3.1}
$$

The sum of frequency component is removed by the low pass filter and with $\omega_R = \omega_S$ we get DC output:

$$
V_O = \frac{1}{2} A_R A_S G_{DC} \cos(\phi_R - \phi_S),
\tag{3.2}
$$

where G_{DC} is the gain in the DC amplifier. The phase of the experimental signal ϕ_S can then be determined by adding $\pi/2$ to the adjusted reference phase ϕ_R that nulls the signal [14, 15, 16].

3.3   Plug and Probe Beams and Time-of-Flight

We set up to do lock-in detection of the atomic beam and time-of-flight measurements as shown in Figure 3.2. The so-called plug beam is MOT light with repump that enters the vacuum chamber slightly before the LVIS mirror as described in Section 2.1.3. This beam pushes the atoms off axis before they reach the exit aperture — in effect, plugging the hole. The intensity of the plug beam is modulated by a 40 MHz AOM. Of course, the AOM also produces a 40 MHz frequency shift to the 20 MHz red beam, so we use the blue shifted order and end up with an intensity modulated beam that is 20 MHz blue. A
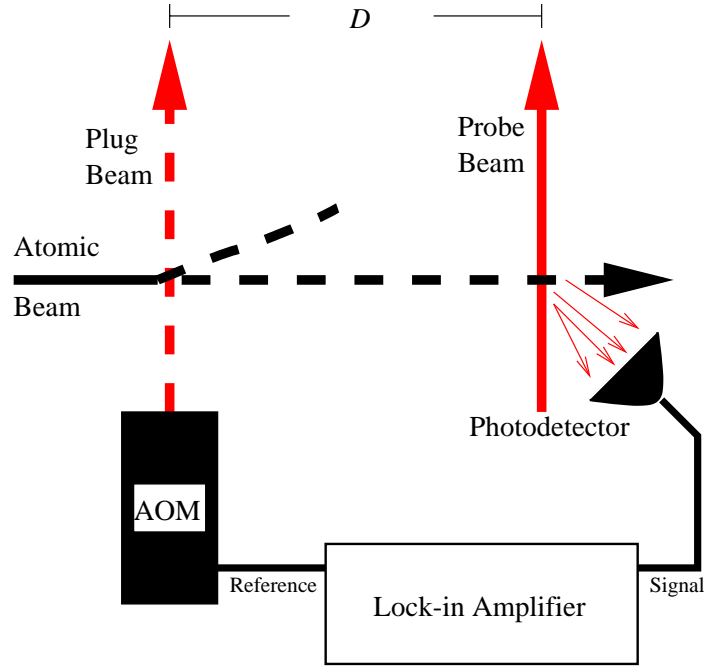
Figure 3.2: Time-of-flight measurement method to determine atom beam velocity distribution. The plug beam is modulated by the AOM and the modulation signal is locked-in with the fluorescence signal.

probe beam may then be used to detect the atomic beam in the chamber following the LVIS mirror aperture. The fluorescence of the atoms in this beam may be collected by a photodetector. Suppose we modulate the plug beam at frequency ω. The detected signal is also at frequency ω and has a phase delay ϕ_S. The delay is due to the time it takes for the atoms to travel the distance D in Figure 3.2. The phase difference may be measured by the lock-in amplifier. It is related to the average velocity as

$$\phi_S = \omega D/\langle v \rangle. \tag{3.3}$$

This could potentially be used to find the average velocity of the atoms.

Unfortunately, we were not able to detect an atomic beam. Several

possible problems could lead to this inability. The problem with the glass cell as discussed in Section 2.1.2 might have prevented the 2D-MOT from working all together. So, perhaps we never had a beam to detect. Another problem was the unfortunate circumstance that we did not have a separate viewport to collect fluorescence. Detection was very difficult.

3.4   Summary and Conclusions

In this work we have described the design and construction of an experimental apparatus for a two-dimensional magneto-optical trap. Simple models of laser cooling and trapping and their relevance were explained in Chapter 1. The possible application of this setup is as a low velocity atomic beam source for loading atom traps.

We discussed in some detail the design of the apparatus and considerations in Chapter 2. In particular, the mirror that is mounted inside the chamber and the magnetic coils are important for the setup. Many details of the optics are found in Section 2.4.

Some parts that were designed and built for this experiment worked very well. For example, current control electronics and the Ioffe coils have been trouble-free from design and construction to implementation. The magnetic fields were mapped out and agree well with theoretical estimates. The holder for the mirror inside the chamber also worked as expected — firmly holding the mirror in place without cracking it during bake-out.

We talked about a few aspects of the construction of this experiment that could be improved. The LVIS mirror, as discussed in Section 2.1.2, ap-

parently changed properties during the chamber bake. Perhaps a mirror with a different coating or a protected metal mirror would work better. The Pyrex cell, discussed in the same section, has problems of scattering light from the windows. A better constructed cell would hopefully avoid these problems as well as those of previous Pyrex cells as pointed out in Section 2.1.2. Finally, another window on the detection chamber would greatly simplify the detection setup.

Appendix

Appendix A

Vacuum Pumps and Gauges

The chamber (as discussed in Section 2.1) has an ion pump and an ionization gauge. The turbo station used in the chamber bake process has a mechanical roughing pump, a turbo pump (hence the station name), a thermocouple gauge, and an ionization gauge.

Thermocouple gauges are useful for measuring pressure in the range of about 1 torr to 10^{-3} torr. The gauge consists of a thermocouple measuring the temperature of a heated filament. The temperature depends on the rate of heat loss to the surrounding gas (i.e. on thermal conductivity). This dependence is nonlinear and the manufacturer generally calibrates the gauges and controllers for air.

Ion gauges are lower pressure devices than thermocouple gauges. They may be used in pressure range of 10^{-3} torr to 10^{-10} torr. These gauges operate by measuring ion current. Electron impact near the gauge ionizes gas particles. The positive ions are then collected at a negative electrode — this is the ion current that is measured. This current is linear with pressure but obviously dependent on the gas present. Standard devices are calibrated for air. Interestingly, ion gauges have a small side effect of being slow pumps.

This is because the ionized particles collected at the electrode are removed from the system.

The pumps on the turbo station are both mechanical pumps. The standard roughing pump is rotary pump that is oil-sealed. These pumps are useful to down to the militorr range. As the name implies, such a pump may be used to 'rough pump' the system down from atmospheric pressure. Far more impressive then the roughing pump is the turbo pump. This pump is also a mechanical pump and is run in series with the roughing pump. In this setup, the roughing pump is true to it's name and pumps through the non-operating turbo pump to rough down the system. After the turbo pump is turned on, the roughing pump works as a backing pump. The turbo pump can be visualized as a fan — but running at $75,000\,\mathrm{rpm}$! Particles in the chamber get a significant mechanical kick towards the backing pump. In effect, the turbo pump is able to hold a pressure difference of 5 to 6 orders of magnitude. This was the device that did the significant pumping during the bakes.

The ion pump operates similar to the side effect pumping of the ion gauge. The pump consists of a stainless-steel anode and a titanium cathode between which there is a magnetically confined discharge. Neutral gas from the chamber is ionized and slams into the titanium cathode removing it from the system. Our pump is a Varian StarCell. It operates at $5,000\,\mathrm{Volts}$ and has a pumping speed of $20\,\mathrm{L/s}$. [15]

Appendix B

Control Circuit Board Layouts

This appendix gives the layouts for the etched boards for the circuits described in Section 2.3. The board layouts were done in EAGLE (Easily Applicable Graphics Layout Editor) from CadSoft. The drawings for the boards were then printed on transparencies with a high resolution laser printer. Boards have a copper layer covered by a photo resist coating. Exposure with a fluorescent lamp for 8 to 10 minutes is sufficient for developing. The developed board may then be etched with ferric chloride solution. The etching fluid produces fine circuit boards.
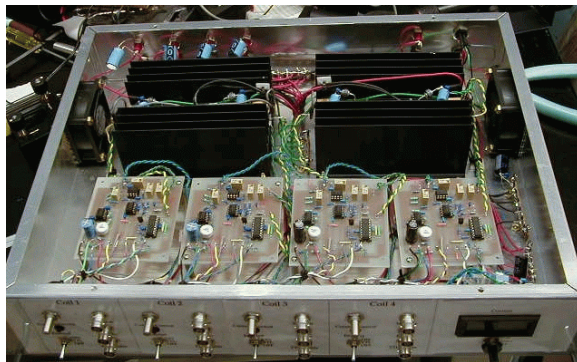

Figure B.1: Photo of the electronics box. Near the front panel are four control circuit boards. On the large heat sinks in the rear of the box are the power circuits.
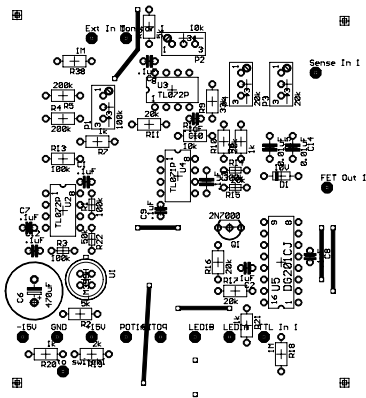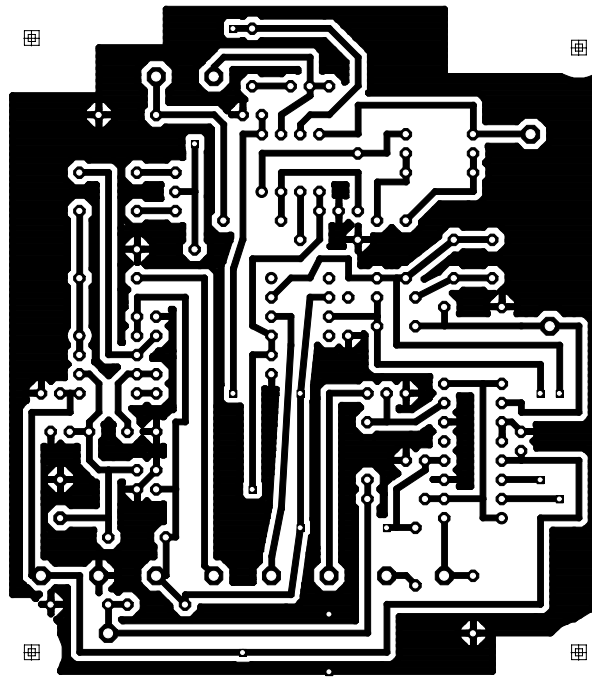
Figure B.2: Control circuit board layout (done in EAGLE by Todd Meyrath). This board has both the control circuit of Figure 2.14 and the voltage reference circuit as in Figure 2.16.
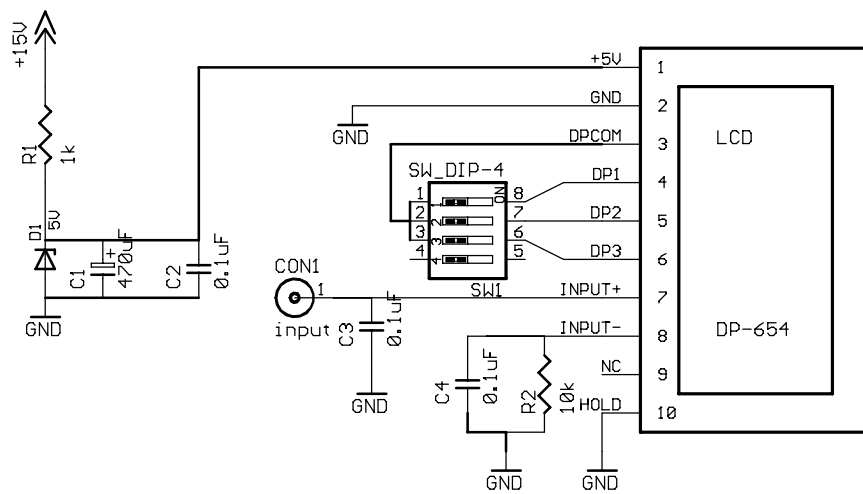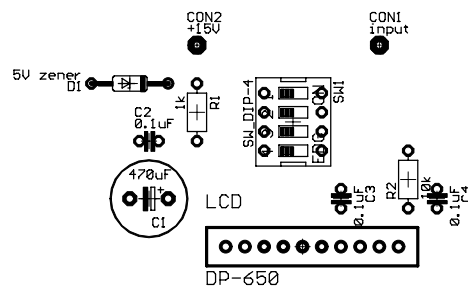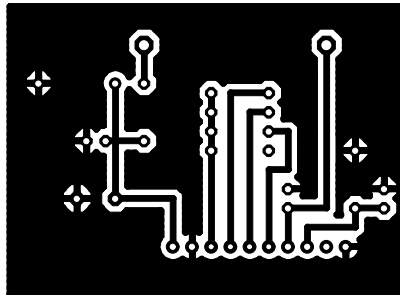
Figure B.3: Circuit for the panel LCD.

Figure B.4: Circuit board layout for the LCD (done in EAGLE by Todd Meyrath). This board serves the simple purpose of supplying the correct supply voltage to the LCD package from the voltage rails in the box. It is mounted on the LCD on the front panel.

Bibliography

[1] K. Dieckmann, R.J.C. Spreeuw, M. Weidemüller, and K. T. M. Walraven: "Two-dimensional magneto-optical trap as a source of slow atoms;" *Physical Review A*, Vol. 58, No. 5, pp. 3891-3895; 1998.

[2] Z.T. Lu, K.L. Corwin, M.J. Renn, M.H. Anderson, E.A. Cornell, and C.E. Wieman: "Low-Velocity Intense Source of Atoms from a Magneto-optical Trap;" *Physical Review Letters*, Vol. 77, pp. 3331-3334; 1996.

[3] C.Y. Park, M.S. Jun, and D. Cho: "Magneto-optical trap loaded from a low-velocity instense source" *Journal of The Optical Society of America B*, Vol. 16, No. 6, pp. 994-997; June 1999.

[4] Dieter Suter: "The Physics of Laser-Atom Interactions;" Cambridge University Press, New York, 1997.

[5] H.J. Metcalf and P. van der Straten: "Laser cooling and Trapping;" Springer, New York; 1999.

[6] W.D. Philips: "Laser Cooling and Trapping of Neutral Atoms;" in *Laser Manipulation of Atoms and Ions* Proceedings of the International School of Physics "Enrico Fermi," Italian Physical Society pp. 289-343; Elsevier Scientific; 1992.

[7] E.L. Raab, M. Prentiss, Alex Cable, Steven Chu, D.E. Pritchard: "Trapping of Neutral Sodium Atoms with Radiation Pressure" *Physical Review Letters*, Vol. 59, No. 23, pp. 2631-2634; 1987.

[8] J. Dalibard and C. Cohen-Tannoudji: "Laser Cooling Below the Dopper Limit by Polarization Gradients — Simple Theoretical-Models;" *J. Opt. Soc. Am. B* **6**, pp. 2023-2045. 1989.

[9] A. Mück: "Recoil-Induced Resonances for Velocimetry of Cold Cesium Atoms" Master's Thesis: Department of Physics, University of Texas at Austin, Austin, Texas. 1999.

[10] D.A. Steck: "Sodium D_2 Line Data;" University of Texas at Austin, Austin, Texas. 2000. *www.ph.utexas.edu/~quantopt*.

[11] R.C. Weast, editor: "CRC Handbook of Chemistry and Physics, 61st Edition 1980-1981;" CRC Press, Inc.; Boca Raton, Florida; 1980.

[12] B.H. Bransden and C.J. Joachain: "Physics of Atoms and Molecules;" Addison Wesley Longman, Essex, England, 1983.

[13] D.J. Griffiths: "Introduction to Electrodynamics" 2nd ed. Prentice Hall, New Jersey; 1989.

[14] P. Horowitz and W. Hill: "The Art of Electronics" 2nd ed. Cambridge University Press, New York; 1989.

[15] J.H. Moore, C.C. Davis, and M.A. Coplan: "Building Scientific Apparatus: A Practical Guide to Design and Construction" 2nd ed. Addison-Wesley; Reading, Massachusetts; 1989.

[16] Stanford Research Systems: "Model SR510 Lock-In Amplifier Manual;" SRS, Inc. Sunnyvale, California. 1989.

Vita

Todd Philip Meyrath was born on August 1, 1975 in Rochester, New York as the son of Frank and Donna Meyrath. He attended Clarke Central High School in Athens, Georgia. In 1998, he was awarded Bachelor of Science in Physics and Bachelor of Science in Applied Mathematics degrees from The Georgia Institute of Technology. He entered The Graduate School of The University of Texas at Austin in August 1998.

Permanent address: 255 Selkirk Ln.
Duluth, Georgia 30097

This thesis was typeset with LATEX‡ by the author.

---

‡LATEX is a document preparation system developed by Leslie Lamport as a special version of Donald Knuth's TEX Program.